*To be submitted (ApJ)* Version, 2000 January 24

# Image Reconstruction of HESSI Data with Forward-Fitting. I. Single and Double Sources

Markus J. Aschwanden and Thomas R. Metcalf
Lockheed Martin Advanced Technology Center, Solar & Astrophysics Laboratory, Dept. L9-41, Bldg.252, 3251 Hanover St., Palo Alto, CA 94304, USA; e-mail: aschwanden@lmsal.com

Ed Schmahl, Richard A. Schwartz, and Brian R. Dennis
NASA Goddard Space Flight Center, Solar & Astrophysics Lab., Greenbelt, MD 20771

Gordon J. Hurford, André Csillaghy, Jim McTiernan, David Smith, Chris Johns-Krull, and Robert P.Lin
Space Sciences Laboratory, University of California, Berkeley, CA 94720

## ABSTRACT

We describe a newly-developed *Forward-Fitting Method* to reconstruct hard X-ray images from the *High Energy Solar Spectroscopic Imager (HESSI)*, a Fourier imager with rotating collimators, planned for a solar flare mission to be launched in July 2000. The forward-fitting method is based on models that represent a spatial map by a superposition of multiple source structures, which are quantified by circular gaussians (4 parameters per source), elliptical gaussians (6 parameters per source), or curved ellipticals (7 parameters), designed to characterize real solar flare hard X-ray maps with a minimum number of geometric elements. We describe and demonstrate the use of the forward-fitting algorithm. We perform some 500 simulations of *HESSI* telemetry files based on models of single and double gaussian sources with random parameters and perform their image reconstruction. We quantify the fidelity of the image reconstruction as function of photon statistics, the accuracy of retrieved source positions, widths, and fluxes, and explore the highest achievable spatial resolution (FWHM $\approx 0.8$"). We address the the convergence behaviour of the algorithm and the uniqueness of the forward-fitting solution.

*Subject headings:* Sun: Corona — Sun : X-rays — Sun : Flares — Instruments — Image Processing — Numerical Methods

## 1. INTRODUCTION

The concept of *rotation-modulated collimators* for Fourier imaging in hard X-rays has a lot of similarity with Fourier synthesis methods in radio interferometry (e.g. Kraus 1966; Hogbom 1974; Gull & Daniell 1978; Cornwell & Evans 1985; Rohlfs 1986). It was first applied to solar flare observations on the Japanese *Hinotori* spacecraft, with imaging in the 20-40 keV energy range and a spatial resolution of 28" (Makishima et al. 1977; Ohki et al. 1982; Enome 1982; Takakura et al. 1983; Tsuneta 1984). The concept has continually evolved over the years and new prototypes were developed (Crannell et al. 1986; 1994; Crannell 1988; Prince et al. 1988; Dennis et al. 1988; Orwig et al. 1989; Hurford 1992; Gaither et al. 1996), resulting in the design of a new high-resolution telescope, the so-called *High-Energy Solar Spectroscopic Imager (HESSI)* (Lin et al. 1993; 1994; 1998; Schmahl & Dennis 1993; Dennis 1994; Dennis et al. 1996a; 1996b; Hurford 1997; Schmahl & Dennis 1997), which was approved as a NASA Small Explorer (SMEX) mission for launch in July 2000. Data analysis from the *HESSI* telescope has been planned and designed for a number of image reconstruction methods (Hurford 1999a, 1999b; 2000; Schmahl 1999a; 1999b, Schwartz 1999; McTiernan 1999; Metcalf 1999; Smith 1999; Csillaghy 1999), including backprojection, cleaning algorithm, maximum entropy method, pixon mapping, polar mapping, and forward-fitting. Image reconstruction with the forward-fitting method is the main subject of this paper.

The Fourier imaging technique, although straightforward by mathematical principles, has to be optimized and analyzed for each instrument individually, because each instrument has a different discrete spacing pattern to sample the Fourier components. In this paper we develop a *Forward-Fitting Method* to produce spatial images from the time-modulated data. We simulate data in anticipation of real HESSI observations, perform image reconstruction, and compare the test results with the input models, in order to quantify the fidelity of the images, the uniqueness of the mathematical solutions, and the noise-induced limits of the image reconstruction method. This information is of over-riding importance for the scientific interpretation of the data.

What is the purpose of imaging with HESSI? HESSI is a solar flare mission. The primary scientific objective is exploring the basic physics of particle acceleration and energy release in solar flares. This will be accomplished by high-resolution imaging at energies of 5 keV through 15 MeV and by high-resolution spectroscopy with cooled germanium detectors, which allow us for the first time to resolve most of the nuclear gamma-ray lines. The germanium detectors will provide sufficiently high energy resolution, i.e. 1 keV below 1 MeV, increasing to 5 keV at 15 MeV. Imaging is accomplished with a set of 9 bi-grid rotating modulation collimators with FWHM resolutions ranging from 2.3" to 183". The unprecedented high spatial resolution and enhanced dynamic range ($\approx$1:100) of HESSI images are expected to reveal the detailed contours of the energy loss regions of accelerated particles, in coronal acceleration sites, in trapping magnetic mirror fields, as well as in chromospheric high-density sites. The detailed mapping, the spatially-resolved energy spectra, and the energy-dependent timing are expected to reveal fundamental insights into the physical processes of particle acceleration, propagation, kinematics, trapping, and energy loss of non-thermal particles, as well as to disentangle the topology and geometry of coronal magnetic reconnection processes.

The content of this paper includes a brief instrumental description (Section 2), the parametrization of images (Section 3), a description of a newly-developed forward-fitting code to reconstruct images from telemetry files of observed or simulated data (Section 4), numerical test results of the image reconstruction from simulated data (Section 5), and a summary (Section 6).

## 2. INSTRUMENT

### 2.1. Instrumental Description of HESSI

Technical descriptions of the HESSI instrument can be found in Lin et al. (1993, 1994, 1998), Dennis et al. (1996), Hurford et al. (2000), and on the HESSI webpage (http://hessi.ssl.berkeley.edu), which contains the most updated information. Here we summarize only some instrumental specifications that are most relevant for image reconstruction. For a detailed description of the imaging capabilities of HESSI, the grid characteristics, the modulation patterns, and modulation profiles we refer to Hurford et al. (2000).

HESSI employs the technique of Fourier-transform imaging with rotating modulation collimators, using a set of 9 bi-grid collimators with a grid period (pitch) ranging from 34 micrometers to 2.6 mm, separated by a distance of 1550 mm between front grid and rear grid. The grid spacing increases by a factor of $\sqrt{3}$ from one grid to the next coarser one, yielding a FWHM resolution ranging from 2.26" to 2.26" $\times \sqrt{3}^8 = 183$". This defines the range of spatial scales over which HESSI is able to map. The full angular resolution of $\approx 2$" is achieved at the lowest energies, up to $\lesssim 300$ keV. At higher energies, where the thickness of the tungsten grids (#2-9) or molybdenum (Mb) grids (#1) is not sufficient to completely absorb high-energy photons, the modulational efficiency is thus reduced, restricting the spatial resolution to the spacing of the thicker, fully-absorbing grids, which is $\approx 20$" above 1 MeV. The angular coverage of an image covers thus 2"-183", while the field of view covers the full Sun, as long as the spacecraft spin axis points somewhere onto the solar disk. The temporal resolution for highest quality images is half a spacecraft rotation period (providing maximum uv-coverage in Fourier space), i.e. 2.0 s, but "snapshot images" with poorer uv-coverage can in principle be obtained down to tens of milliseconds. The pointing of the spacecraft is controlled by a *Solar Aspect System (SAS)* which determines the direction to Sun center to $< 1.5$", and by a *Roll angle Aspect System (RAS)*, which determines the roll angle to $< 3$ arcminutes. Great care has been taken to warrant that the relative twist of the finest grid pair is maintained to within one arcminute by the metering tube structure. Spectroscopy of hard X-rays and gamma rays is achieved with internally segmented germanium detectors (GeDs), placed behind the bi-grid collimators, having diameters of 71 mm and a length of 85 mm. The germanium detectors are cooled down to 80 K, providing $< 1$ keV FWHM energy resolution at 10 keV, increasing to 5 keV at 20 MeV.

### 2.2. Data Structure of Observations

HESSI will record every photon above a threshold energy of $\gtrsim 5$ keV as a time-tagged event up to a maximum rate of $\approx 10^6$ s$^{-1}$, while decimation schemes are planned at higher rates to avoid pulse pileup effects. Thus, the telemetry data will contain photon event lists from each of the 9 detectors, tagged with a time accuracy of 1 microsecond (called *Photon Event List*. This list of time-tagged photon events is the data structure of the telemetry files.

For standard image processing, the time-tagged photon events will be binned into histograms with time intervals that resolve the grid-induced modulation due to the spinning spacecraft. The number of modulations per rotation depends on the angular distance $r$ of the observed source from the spacecraft spin axis, divided by the pitch angle $p_l = 4.52" \sqrt{3}^{l-1}$ of the detector ($l = 1, ..., 9$),

$$N_l^{mod} = \frac{4r}{p_l} = \frac{0.88r"}{\sqrt{3}^{l-1}} \ , \qquad l = 1, ..., 9 \ . \tag{1}$$

For a maximum field-of-view of $r \le 1^0$ we record $N_1^{mod} = 3185$ modulations for the finest detector and $N_9^{mod} = 39$ modulations for the coarsest detector. The required time binning to resolve at least 2 data points per modulation is thus

$$\Delta t_l^{mod} = \frac{T^{rot}}{2N_l^{mod}} = 0.6 \left( \frac{r"}{3600"} \right)^{-1} \sqrt{3}^{l-1} \ \mathrm{ms} \ , \qquad (2)$$

ranging from $\Delta t_1^{mod} \gtrsim 0.6$ ms for the finest detector to $\Delta t_9^{mod} \gtrsim 50$ ms for the coarsest detector, for a spacecraft spin period of $T^{rot} = 4.0$ s. The actual binning of the data is done by the nearest numbers of powers of 2, i.e. the default number of binning intervals varies from 128 (Detector 9) to 8192 (Detector 1), and the corresponding time intervals range from 0.5 ms (Detector 1) to 32 ms (Detector 9). The values of the detector pitch angles $p_l$ and the default time binning $\Delta t_i$ are listed in Table 1. Thus the typical data structure used for image processing consists of 9 arrays of *modulation profiles* $N_l^{obs}(t_k)$ for the detectors $l = 1, ..., 9$ with variable number of time bins, $t_k =, 1., , , , .N_l$, ranging from $N_1 = 8192$ to $N_9 = 128$, amounting to a total of $\sum_{l=1}^{9} N_l = 17,792$ data points per spacecraft rotation. This data format of binned photon counts, which also includes several instrument calibration procedures, is called *Calibrated Event List* in the HESSI jargon.

## 3. PARAMETRIZATION OF MAPS

The simulation of maps, $I(x, t)$, as well as the forward-fitting method require a parameterization of the geometry of source morphologies. HXR sources in solar flares are known to appear as (often unresolved) point sources, double sources, multiple sources, or parts of flare loops (Sakao 1994; see also *Yohkoh/HXT Image Catalogue* by Kosugi et al. 1995, and Sato et al. 1998). We adopt the philosophy that such maps can mathematically be represented as a superposition of a few elementary geometric shapes.

### 3.1. Geometry of Elementary Source Structures

The simplest shape is a point source, placed at location $(x_i, y_i)$, with a flux amplitude $f_i$. Every point source has also a finite width, regardless whether this width represents the physical extent of the source or the apparent size of an unresolved source, as rendered by the instrumental point-spread function. Thus, it is most natural to characterize a point source with a gaussian width $w_i$, so that their 2-dimensional distribution in a map is defined by 4 parameters $(x_i, y_i, f_i, w_i)$,

$$F(x, y) = f_i \exp \left[ - \frac{(x - x_i)^2 + (y - y_i)^2}{2w_i^2} \right] \ . \qquad (3)$$

In a next step we generalize a circular gaussian geometry to an elliptical shape, which can be defined by two additional parameters, the eccentricity $e_i$ and the tilt angle $\alpha_i^{tilt}$. We define the eccentricity by the ratio of the ellipse half-axis $w_i^x$ along the x-axis to the half-axis $w_i^y$ along the y-axis (Fig.1 top), and subtract a constant that makes the eccentricity zero for circular symmetry, i.e.

$$e_i = \left( \frac{w_i^x}{w_i^y} - 1 \right) \ . \qquad (4)$$

The 2-dimensional distribution of an elliptical gaussian is then

$$F(x", y") = f_i \exp \left[ - \frac{(x" - x_i)^2}{2w_i^2} - \frac{(y" - y_i)^2}{2w_i^2} (e_i + 1)^2 \right] \ . \qquad (5)$$

To obtain the 2-dimensional distribution of an elliptical gaussian in an arbitrary orientation, the coordinates (x”,y”) aligned with the elliptical major and minor axes have to be rotated by the tilt angle $\alpha_i^{tilt}$ (defined anti-clockwise with respect to the x-axis),

$$x = x\text{”} \cos(\alpha_i^{tilt}) - y\text{”} \sin(\alpha_i^{tilt}) \quad (6)$$

$$y = x\text{”} \sin(\alpha_i^{tilt}) + y\text{”} \cos(\alpha_i^{tilt}) \; . \quad (7)$$

In order to provide geometric elements that can represent loop-like shapes we go a step further and introduce curved gaussians, which require only one additional parameter, the curvature radius $r^{curv}$. It is mathematically more convenient to choose the reciprocal curvature radius, because this way we have no singularity $r^{curv} = \infty$ for uncurved ellipticals or gaussians, and this additional parameter is then zero if no curvature is wanted. We define a dimensionless parameter $\rho_i^{curv}$by the ratio of the gaussian width $w_i$ along the x-axis to the curvature radius $r_i^{curv}$,

$$\rho_i^{curv} = \frac{w_i}{r_i^{curv}} \; . \quad (8)$$

For coordinate transformations from curved ellipse coordinates $(x\text{”}, y\text{”})$ into cartesian coordinates $(x, y)$ it is most convenient to use the rotation angle $\alpha^{curv}$ that measures the x-position on the curved x-axis with respect to the curvature center (Fig.1, top right),

$$\alpha^{curv} = \frac{x\text{”}}{r_i^{curv}} = \frac{x\text{”}}{w_i} \rho_i^{curv} \quad (9)$$

The transformation from curved ellipse coordinates $(x\text{”}, y\text{”})$ into cartesian coordinate $(x', y')$ is then simply

$$x' = (r_i^{curv} + y\text{”}) \sin(\alpha^{curv}) \quad (10)$$

$$y' = (r_i^{curv} + y\text{”}) \cos(\alpha^{curv}) \quad (11)$$

With a subsequent rotation by the orientation angle $\alpha_i^{tilt}$, the cartesian ellipse coordinates $(x', y')$ can then be rotated into the cartesian reference system $(x, y)$ (by substituting $(x', y')$ from Eqs.10-11 into $(x\text{”}, y\text{”})$ of Eqs.6-7).

### 3.2. Map Parameterization

We have now defined the general geometry of a single source with 7 free parameters, which has the morphology of a curved gaussian in the most general form, but can be reduced to 6 free parameters (in the form of an elliptical gaussian without curvature), or to 4 parameters (in the form of a circular gaussian). The geometry of these three shapes can be described with the same general 7-parameter formalism $(x_i, y_i, f_i, w_i, e_i, \alpha_i^{tilt}, \rho_i^{curv})$, while setting a subset of the last three parameters to zero will automatically reproduce the simpler shapes.

We define a map simply by a superposition of the 2-dimensional distributions $F_i(x, y; P_i)$ of the elementary shapes defined by the parameter sets $P_i = [x_i, y_i, f_i, w_i, e_i, \alpha_i^{tilt}, \rho_i^{curv}]$,

$$F(x, y) = \sum_{i=1}^{n^g} F_i(x, y; P_i) \quad (12)$$

with $n^g$ the number of gaussian sources (or elementary shapes). The total number of free parameters of such a parametrized map is

$$n^{free} = n^g \times n^{par} - 1 \quad (13)$$

where $n^{par}$ represents the number of parameters per source (i.e. $n^{par} = 4$ for circular gaussians, $n^{par} = 6$ for elliptical gaussians, and $n^{par} = 7$ for curved gaussians). The total number of free parameters is reduced by 1, because the total flux of the map can be normalized to unity ($I^{norm}(x,y) = I(x,y) / \int I(x,y)dxdy$), having the physical unit of 1 photon count per map. The total number of photons can directly be obtained by summing the time profiles, $N_l^{phot} = \sum_{k=1}^{N_l} N_l^{obs}(t_k)$ for each detector $l = 1, ..., 9$. A map in physical units of photons per pixel and detector (or subcollimator) can then simply be retrieved by scaling the normalized map with the averaged photon number per detector, i.e. $I(x,y) = I^{norm}(x,y) \times < N_l^{phot} >$.

Some examples of such parameterized maps are shown in Fig.1, including a single point source (3 parameters), a double source (7 parameters), a double source with a loop (14 parameters), and a Masuda-type flare (Masuda et al. 1994) with an additional above-the-loop-top source (18 parameters).

## 4. FORWARD-FITTING ALGORITHM

We describe now the mathematical and numerical formalism of the basic *forward-fitting method* as currently implemented in the HESSI software (HESSI release 4, status of January 2000), a package of the *Interactive Data Language (IDL)*-based *Solar SoftWare (SSW)* (Freeland & Handy 1998).

### 4.1. The Basic Steps of the Algorithm

The algorithm is basically defined by the input, which consists of a list of time-tagged photon events from the 9 detectors (packed in telemetry files) and the desired output in the form of a reconstructed map $I(x,y)$, which, ideally, should be consistent with the observed time profiles, within the expected photon count noise. The algorithm consists of 10 basic steps (Fig.2). For the simulations here, an additional step is required beforehand, which includes the simulation of telemetry files from a model map (numbered as step "0" in the following scheme).

*Step 0:* Selection of a set of model parameters $P_i, i = 0, ..., n^{free}$ that define a model map $I^{model,sim}(x,y)$. Simulation of a list of photon events that are randomly distributed in time and reproduce the spatial 2D distribution prescribed by the model map. The time-tagged photon events are written out into telemetry files that have the same format as observations telemetered down from the spacecraft.

*Step 1:* Time intervals $[t_1, t_2]$, energy intervals $[E_1, E_2]$, image size $[N_x, N_y]$, image offset from Sun center $[X_{offset}, Y_{offset}]$, and pixel resolution $\Delta x$ are selected for desired image reconstruction.

*Step 2:* From the telemetry files, a calibrated (binned) event list is created, $N^{obs}(t_k, D_l)$ (for time bins $t_k$ and detectors $D_l, l = 1, ..., 9$), and the corresponding modulation patterns are calculated, $DRM_{ijkl}$ (for each pixel $x_i, y_j$).

*Step 3:* A *back-projection* is performed from the calibrated event list to obtain an initial first-guess map $I^{BP}(x,y)$ for the forward-fitting procedure.

*Step 4:* The back-projection map $I^{BP}(x,y)$ is decomposed into circular source components in order to determine a first-guess value of the number $(n_g)$ of gaussian components and their spatial positions, which are used to specify an initial set of gaussian parameters $P_i, i = 0, ..., n^{free}$ (for a small number of gaussian source components).

*Step 5:* Based on the first-guess gaussian parameters $P_i, i = 0, ..., n^{free}$, a first model map $I^{model1}(x, y)$ is composed, which provides the input for the first iteration of the *forward-fitting* procedure. We normalize the model map to 1 photon count per image, i.e. by $I^{model1,norm}(x, y) = I^{model,1}(x, y) / \int I^{model1}(x, y) dx dy$

*Step 6:* The first model map $I^{model1}(x_i, y_j)$ is multiplied with the detector response matrix $DRM_{ijkl}$ to obtain the modulation time profile

$$MP^{model1}(t_k, D_l) = DRM_{ijkl} \otimes I^{model1,norm}(x_i, y_j) \ , \tag{14}$$

which is then scaled into the same physical units as the observed time profiles, i.e. counts per time bin,

$$N^{model1}(t_k, D_l) = R^{phot} \Delta t(D_l) q^{trans}(D_l) MP^{model,1}(t_k, D_l) \ , \tag{15}$$

where $R^{phot}$ represents the photon count rate per sec and subcollimator (s$^{-1}$ SC$^{-1}$), $\Delta t_k(D_l)$ is the time bin used for detector $D_l$, and $q^{trans}(D_l)$ is the bi-grid transmission factor of detector $D_l$.

*Step 7:* The $\chi^2$ or C-statistic (see Appendix A) is calculated between the observed time profiles $N^{obs}(t_k, D_l)$ and the model time profiles $N^{model1}(t_k, D_l)$,

$$\chi^2 = \frac{1}{n_{t'}} \sum_{k'=1}^{n_{t'}} \frac{[N^{obs}(t_{k'}) - N^{model}(t_{k'})]^2}{[\sigma^{model}(t_{k'})]^2} \ , \tag{16}$$

where the time series $t_k$ from each detector $D_l$ are concatenated $[t_{k'} = t_k(D_1), ..., t_k(D_9)], k' = 1, ..., n_{t'}$ to obtain a single $\chi^2$ or C-statistic value for a given image. (An alternative is to average the $\chi^2$'s from each detector).

*Step 8:* The parameters $P_i, i = 0, ..., n^{free}$ are varied in all $(n^{free})$ dimensions and the change of $\chi^2$ or C-statistic, $\Delta C = C(P_i + \Delta P_i) - C(P_i)$, is calculated. A new parameter set $P_i^{new} = P_i - \Delta P_i(\partial C / \partial P_i)$ is calculated from the steepest gradient of $\chi^2$ in the $n^{free}$-dimensional parameter space, so that the new parameter set $P_i^{new}$ points into the direction where $C$ decreases strongest. The search for a local minimum in direction of the steepest gradient is performed by increasing the steps $\Delta P_i$ by powers of 2 and using a cubic spline fit of $C(P_i^{new})$. The set of parameters $P_i^{new}(min[C])$ associated with the local minimum of $C$ is used as starting point for the next iteration cycle of the forward-fitting procedure.

*Step 9:* The next model map $I^{model2}(x_i, j_i)$ is calculated based on the new parameter set $P_i^{new}, i = 0, ..., n^{free}$ and steps 6-8 are repeated iteratively until the change in $C$ converges, e.g. $\Delta C < 10^{-4}$ per iteration cycle.

*Step 10:* After $n$ iterations, the final map $I^{model,n}(x, y)$ becomes the solution of the desired reconstruction of a spatial map. In the case of simulations, the final map $I^{model,n}(x, y)$ can be compared with the initial model $I^{model,sim}(x, y)$ used for creating the telemetry files (Step 0) to verify the fidelity of the reconstruction. In the case of real observations, the final solution may be compared with other reconstruction methods (such as cleaning or maximum entropy). A self-consistency criterion between the reconstructed model map and the observations is the convergence value of $\chi^2$ or C-statistic, which should have values near unity, say within $\lesssim 10\%$. If the $\chi^2$ or C-values are significantly above unity, (provided there is no convergence problem to the global minimum), this would indicate that the model parametrization is not adequate to represent the data, and thus requires a more complex model.

This outline is only a formal description of the basic steps of the forward-fitting code (Fig.2). To understand the most efficient implementation, the accuracy and limitations of the solutions, and the convergence behaviour of the algorithm, we provide more detailed information in the following subsections.

### 4.2. Data Noise and Detector Selection

It is a property of every well-behaving image reconstruction algorithm that parameter changes are most significant in the first iteration steps, while latter iterations near the convergence limit are less efficient and essentially are dominated by data noise. In the case of forward-fitting in particular, it is desirable to suppress those computation-expensive parts of the calculations which bluntly fit the data noise. A first important efficiency consideration is therefore to select only those detectors that have a reasonable signal-to-noise ratio to be sensitive to the fitting algorithm.

For the HESSI detectors, the time profiles of the finest detectors are naturally the noisiest ones, because the same number of photons (per detector) is spread out over a larger number of time bins (by the requirement of resolving the rotational modulation). The signal-to-noise ratio, say $S/N \approx N^{phot}/\sqrt{N^{phot}} = \sqrt{N^{phot}}$, is worse for the finer detectors, because it decreases as $S/N \propto \sqrt{\Delta t_i^{bin}}$ with decreasing time bin length $\Delta t_i^{bin}$. For instance, if the coarsest detector has a signal-to-noise ratio of 100:1, it will be 12:1 for the finest detector, because the time bins vary by a factor of $\Delta t_9^{bin}/\Delta t_1^{bin} = 64$.

In order to decide which time profiles can be ignored in the forward-fitting procedure without significant loss of information, we define a significance criterion that is expressed by the ratio of its standard deviation $\sigma^{rms}$ to the expected data noise $\sigma^{noise}$. The r.m.s. fluctuation of a time profile $N^{obs}(t_k, D_l)$ is composed of the variability due to the rotational modulation $\sigma^{mod}$ and the photon count statistic noise $\sigma^{noise}$,

$$(\sigma^{rms})^2 = (\sigma^{mod})^2 + (\sigma^{noise})^2 \tag{17}$$

For instance, when the variability due to rotational modulation, $\sigma^{mod}$, falls below 20% of the counting noise, $\sigma^{noise}$, the combined r.m.s. variability, $\sigma^{rms} = \sigma^{noise} \times \sqrt{1 + 0.2^2} = 1.02\ \sigma^{noise}$, exceeds the data noise only by 2%. Any fitting method based on a $\chi^2$-criterion becomes quite insensitive at this level, because $\chi^2 \propto (\sigma^{noise})^{-2}$ (Eq.16) varies then only by 4%, which has little significance in judging the goodness of a fit. Therefore, we adopt a threshold criterium of

$$(\frac{\sigma^{rms}}{\sigma^{noise}}) \ge 1.02 \tag{18}$$

to select detectors that have time profiles with significant modulation in the forward-fitting procedure. This criterion is equivalent to

$$(\frac{\sigma^{mod}}{\sigma^{noise}}) \ge \sqrt{(1.02^2 - 1)} = 0.2\ . \tag{19}$$

The average counts per time bin is $N_l^{obs} = R^{phot} \Delta t_l q_l^{trans}$ (see Eq.15), while the total number of events in the time interval $(t_2 - t_1)$ is $N_l^{tot} = R^{phot}(t_2 - t_1) q_l^{trans}$. Applying Poisson statistics for a binomial distribution with $n = N_l^{tot}$ events and a mean of $< x >= N_l^{obs}$ in the limit of small probabilities $(p =< x > /n)$, which is the case here since

$$p = \frac{< x >}{n} = \frac{N_l^{obs}}{N_l^{tot}} = \frac{\Delta t_l}{(t_2 - t_1)} \ll 1\ , \tag{20}$$

the standard deviation from the mean is $\sigma = \sqrt{< x >}$ for $p \ll 1$ (Bevington 1969, p.33), and thus

$$\sigma_l^{noise} = \sqrt{N_l^{obs}} = [R^{phot} q_l^{trans} \Delta t_l]^{1/2}. \tag{21}$$

In Fig.3 we compare the r.m.s. noise $\sigma_l^{noise}$ with the r.m.s. fluctuations due to rotational modulation $\sigma_l^{mod}$, which is

$$\sigma_l^{mod} \approx 0.5\ \varepsilon_l^{mod} N_l^{obs} \tag{22}$$

for the 9 detectors ($l=1,...,9$) and modulation efficiency $\varepsilon_l^{mod}(\le 1.0)$. From the requirement that the variability due to rotational modulations exceeds the data noise by 20% (Eq.19), we can infer a requirement for a minimum photon rate to produce significant modulations in the detectors. Combining Eqs.19-22 we find

$$N_l^{obs,min} \ge (\frac{0.2}{0.5\varepsilon_l^{mod}})^2 = \frac{0.16}{(\varepsilon_l^{mod})^2} \ , \tag{23}$$

which yields a minimum photon rate $R_l^{min}$ of

$$R_l^{min} \ge \frac{N^{obs,min}}{q_l^{trans}\Delta t_l} \approx \frac{10^3}{\sqrt{3}^{l-1}} \tag{24}$$

These limits are indicated in Fig.3 and tabulated in Table 2, ranging from $R_1^{min} \ge 900$ cts s$^{-1}$ SC$^{-1}$ for the finest detector #1 to $R_9^{min} \ge 17$ cts s$^{-1}$ SC$^{-1}$ for the coarsest detector #9. These count rate limits are derived for 100% modulation efficiency, but would be higher for source sizes that are comparable or larger than the grid pitch, where the modulation efficiency drastically drops.

The count rate limits $R_l^{min}$ for different detectors $l$ (indicated in Fig.3 and listed in Table 1) save a lot of computational effort. For instance, if a weak flare with a relatively low count rate of $R^{phot}=100$ cts s$^{-1}$ SC$^{-1}$ is observed, we see immediately (Table 2) that this count rate is below the requirement $R_l^{min}$ of significant modulation for detectors #1-5. We need therefore only to consider detector #6-9 for image reconstruction. The number of time bins from detectors #6-9 is $\sum_{i=6}^{9} N_i^{bin} = 1408$, and thus a factor of $(17,792/1408) = 12.6$ smaller compared with the number of time bins from all detectors #1-9, making the computation a factor of $\approx 12$ faster (since the computation of modulation profiles scales linearly with the number of time bins).

### 4.3. Decomposition of Backprojection Maps

For the first guess of source positions in the forward-fitting algorithm we make use of a backprojection map. *Back-projection* is a basic imaging method suitable for rotational aperture synthesis in X-rays (Mertz, Nakano, & Kilner 1986). The back-projection method essentially consists of a superposition of modulation patterns at rotation angle $\varphi_k$ for each time-tagged photon recorded at phase angle $\varphi(t_k) = 2\pi(t_k/T^{rot})$. The result is a *dirty map* that shows a very broadened flux distribution at the locations of the true sources, and it has been shown that back-projection produces the statistically best estimate of the source position. Therefore we employ the back-projection method to obtain an initial guess of the source positions $(x_i, y_i)$ before we start forward-fitting.

The backprojection maps have a number of well-understood artifacts, they are not the cleanest or simplest possible map representing the true source. If the collimator phase is constant during rotation, the backprojection map shows a fictious source at the spin axis position due to the lack of modulation at that point. The collimator phase will almost certainly not be constant for HESSI, so the spin axis will be washed out. There is a fictious "mirror" source in backprojection maps at a position symmetric to the true source relative to the spin axis. The sign of the mirror source depends on the collimator phase, and its variations will also wash it out with respect to the true source. The rings around the source in backprojection maps have radii and spacing that depend on the collimator pitch. Adding the maps from several collimators therefore tends to smooth out the rings, while reinforcing the true source.

Our algorithm to derive estimates of source positions $(x_i, y_i)$ from backprojection maps consists of an iterative decomposition of the strongest peaks in a backprojection map. The exact peak location $(x_i, y_i)$ is determined with sub-pixel accuracy by parabolic interpolation of the maximum in both x- and y-direction. Because ring structures around a peak are an artifact of the backprojection map, we subtract also concentric rings around each peak, with an amplitude that corresponds to the median flux value averaged around the ring. Rings with small radii have also higher fluctuations in their azimuthal flux due to the discreteness of the collimator pitches. To avoid misidentification at such azimuthal fluctuations as possible source locations, we exclude smaller rings by requiring a minimal distance between (true) source positions. This criterion should be chosen based on the expected separation between dominant HXR sources, e.g. $d^{min} \gtrsim 10" - 25"$ for flareloop footpoints.

In Fig.4 we show an example of the decomposition of two gaussian sources from a backprojection map. The $64 \times 64$ pixel map has a pixel size of 2". The dominant source is found at a position of $(x_1, y_1) = (14.7", 13.3")$, which is 1.1" away from the true source position $(14.4", 14.4")$. The first gaussian component contains 94.7% of the total flux of the backprojection map. The residual map after subtraction of the first gaussian component is shown in Fig.4 (second row, left). From the peak in the first residual map, the second gaussian component is located, at position $(x_2, y_2) = (20.9", 2.9")$, which is 4.0" away from the true source position $(20.0", 0.0")$. The flux contained in the second gaussian is only 1.7%. The remaining residuals contain 3.6% of the flux and are dominated by the mirror source of the first gaussian.

### 4.4. Field-of-View and Pixel Size Selection

The computation of modulation patterns, i.e. the detector response matrix $DRM_{ijkl}$, is the most expensive computational part, while modulation profiles $MP(t_k, D_l)$ are computed by a simple matrix multiplication, $MP(t_k, D_l) = DRM_{ijkl} \otimes I(x_i, y_j)$, the next most expensive computational effort. Both computational procedures scale with the number of image pixels $N_x \times N_y$. The computation time is therefore most efficient for a small field-of-view $x^{FOV}$ and a large pixel size $\Delta x$, both minimizing the number of pixels, $N_x = x^{FOV}/\Delta x$. For instance, the computational effort for a $64 \times 64$ grid with a pixel size of 1" is 16 times larger than covering the same field-of-view with a $16 \times 16$ grid with a pixel size of 8". Because the source positions can be determined with an accuracy of $\lesssim 10\%$ of a pixel size for sufficiently high count rates, we can still achieve $\lesssim 1"$ accuracy with an 8" pixel size. However, if the source size is significantly smaller than 8", the source would be unresolved with this grid and image reconstruction would render broadened sources with smaller amplitudes. Such cases can, however, easily be recognized when the forward-fitting code yields source sizes smaller than the pixel size, in which case the forward-fitting can be repeated with smaller pixel sizes and perhaps reduced field-of-view. For efficient use of the forward-fitting code we recommend starting with a $16 \times 16$ grid and a pixel size of 8". The resulting field-of-view is then $x^{FOV} = N_x \times \Delta x = 128"$.

We implemented a self-adjusting pixel-size in the forward-fitting code to optimize the field-of-view with respect to the actual image area that is covered by source structures. Because the positions $(x_i, y_i)$ of gaussian sources can be measured fairly accurate from backprojection maps, and an upper limit of the source width $w_i$ can be estimated from the FWHM resolution ($\alpha_l^{res} = \alpha_l^{pitch}/2$, see Table 1), the maximum distance $r^{max}$ of gaussian sources $i = 1, ..., n^g$ from the image center, including a tail of 5 gaussian widths, is

$$r^{max} \lesssim max[\sqrt{x_i^2 + y_i^2} + 5w_i] \qquad i = 1, ..., n^g \ . \tag{25}$$

We adjust then the field-of-view to this required maximum distance $r^{max}$ by varying the pixel size correspondingly (keeping the same grid raster, e.g. $16 \times 16$). If the gaussian sources are localized close together, the pixel size shrinks and a higher resolution is gained. If the gaussian sources are close to the border of the initially chosen image or if the source widths are found to be large, the field-of-view is automatically expanded without requiring more computational effort. In particular for cases with large source widths this automated expansion is very efficient and provides the same relative accuracy. Only in the case of small but distant sources, the pixel size has to be decreased on the expense of additional computational effort.

### 4.5. Parameter Optimization in Forward-Fitting

The forward-fitting method essentially consists in the optimization of $n^{free}$ parameters until the modulation time profiles resulting from the model map (constrained by $n^{free}$ gaussian parameters) are consistent with the observed time profiles $N^{obs}(t_k, D_l)$. For simple maps, e.g. the examples shown in Fig.1, this task consists in the optimization of 3-18 free parameters, which requires substantially less computing effort than standard Fourier image reconstruction methods (e.g. cleaning, maximum entropy), where the number of free parameters scales with the number of map pixels, $N_x \times N_y$. The forward-fitting method is therefore expected to perform faster then standard Fourier imaging methods, with the only disadvantage that the model parametrization may be inadequate for real maps with complex morphologies. In principle, however, any brightness distribution $I(x, y)$ of a real map can be represented by a finite number of gaussians, in the worst case by $N_x \times N_y$ components, which essentially is equivalent to the map representation in the clean algorithm (Hogbom 1974). Here we restrict to a very small number of source components, say 1-4 gaussian components. The number of free parameters to be optimized varies therefore in the range of $n^{free} = 3 - 27$ for $n^{par} = 4 - 7$ free parameters per source. In the following we describe the optimization in the $n^{free}$-dimensional parameter space.

The minimization of the $\chi^2$ or C-statistic of a parameter set $(P_i), i = 1, ..., n^{free}$ requires the calculation of a modulation profile $N^{model}(t_k, D_l)$ for each new trial of a model map $I(x, y; P_i)$, in order to calculate the $\chi^2$ or C-statistic of a new parameter set $(P_i)$. We develop a variant of the multi-dimensional *downhill simplex method* (Press et al. 1986, p.289) that requires a small number of modulation profile computations. The most efficient multi-dimensional minimization algorithms involve the analytical formulation of the derivative $\partial\chi^2/\partial P_i$ (or $\partial C/\partial P_i$ in the case of C-statistic), which is not tractable for the calculation of modulation profiles here. Therefore, we resort to a numerical calculation of the steepest gradient,

$$\nabla C := \frac{\partial C}{\partial P_i} = \frac{C(P_i + \Delta P_i) - C(P_i)}{\Delta P_i} \ , \tag{26}$$

requiring $n^{free}$ computations of modulation profiles for one gradient value. The direction of the steepest decrease of $C$ follows in the opposite direction to the steepest local gradient $\nabla C$. A new parameter set $(P_i^{new})$ in direction to the local minimum can then be specified by

$$P_i^{new,1} = P_i - \frac{\nabla C}{max|\nabla C|}. \tag{27}$$

The minimum of $C(P_i)$ in the direction of the steepest gradient can be large (i.e. at the first iteration steps) or very small (during the latest iteration steps). In order to cover this variable distance in the most efficient way we enlarge the steps by powers of 2,

$$P_i^{new,j} = P_i - \frac{\nabla C}{max|\nabla C|} \times 2^{(j-1)}. \tag{28}$$

where $j = 1, ..., n_j$ is covers as many steps as are required to cross the valley and ascend up to the same height as the original starting point, i.e. until $C(P_i^{new,n_j}) > C(P_i)$. From this set of $n_j$ trial values $P_i^{new,j}$

which cover the valley across a local minimum, we determine the exact value of the local minimum by a cubic spline fit through $C(P_i^{new,j}), j = 1, ..., n_j$, yielding a best new value $C(P_i^{new})$. Thus, such an iteration cycle requires $n^{free} + n_j + 1$ computations of modulation profiles. The number $n_j$ does not exceed 10 at the beginning (because $(P_i^{true} - P_i^{guess})/\Delta P_i = 2^{n_j} \ll 10^3$), and approaches $n_j = 3$ in the final iterations. After a new parameter set $P_i^{new}$ has been evaluated, we repeat the same procedure (Eqs.26-28) until the $\chi^2$ or C-statistic converges, say to a finite small difference of $(C^{new} - C^{old}) \le 10^{-4}$ in subsequent iteration cycles. This level of convergence is reached typically after a few ( $\lesssim 10$) iteration cycles.

## 5. NUMERICAL TESTS AND RESULTS

In this study we provide test results from some 500 simulations where forward-fitting has been performed. The simulations are restricted here to 1 and 2 circular gaussian sources, encompassing thus 3 and 7 free parameters. Additional simulations with triple and more sources, as well as simulations with non-circular sources (elliptical, curved ellipticals) are subject of future studies.

### 5.1. Example of a Simulation

An example of the simulated data is given is Fig.5, where the telemetry files where simulated with a photon count rate of $R = 23,777$ cts s$^{-1}$ and a time interval of $t_2 - t_1 = 4.0$ s, having a spatial distribution specified by two gaussians at positions $(x_1, y_1) = (26.0", -22.0")$ and $(x_2, y_2) = (-22.0", -6.0")$, relative fluxes of $(f_1, f_2) = (1.0, 0.6)$, and relative widths of $(w_1, w_2) = (7.7", 8.3")$. The center of the map is located at an offset of $(X_{offset}, Y_{offset}) = (600", 200")$ from the spin axis at the Sun center. (This is a default offset used in all simulations here). The model map is shown in the top middle panel, and the solution of the forward-fitting algorithm in the top left panel, while the difference is visualized in the third top panel. Fig.5 shows the 7 time profiles $N_l^{obs}(t_k)$ of the detectors $l = 3, ..., 9$, while the detectors $l = 1, 2$ were found to have insignificant modulation ($\sigma^{rms}/\sigma^{noise} < 1.02$; Eq.19), and thus were discarded in the forward-fitting. The C-statistic is given for each detector separately (in the panels of the time profiles), while the averages and standard deviations of the C-statistic ($C^{fit} = 1.060 \pm 0.127$ and $C^{sim} = 1.064 \pm 0.125$) are listed at the top left corner of Fig.5. Note that the difference of the $C$-values is only $\Delta C = C^{fit} - C^{sim} = -0.003 \pm 0.003$ between the best-fit and the expected value of the model. The best-fit time profiles (black lines) lay exactly on top of the time profiles expected from the model (grey curves), overlaid on the observed time profiles $N_l^{obs}(t_k)$ (histogrammed curves), and thus demonstrate that the code converged to the very same solution (within the uncertainties of the data noise). The best-fit and model gaussian parameters are also explicitely listed under each map.

### 5.2. Simulation of Single Sources

We perform now a series of 12 simulations with a single source, by varying the photon count rate from $R = 20, 50, 100, 200, ...,$ to 100,000 cts s$^{-1}$ SC$^{-1}$, but keeping all other parameters constant, i.e. the gaussian width $w_1 = 8"$, the centroid position $(x_1 = -25", y_1 = 25")$. We show the time profiles for Detector #6 (Fig.6, left) for 6 different cases to illustrate the goodness of the fits for sparse to dense sampling. For the case with most sparse sampling at $R = 20$ cts s$^{-1}$ SC$^{-1}$ (Fig.6 left top), many time bins have zero counts, leading to a value of the C-statistic less than unity (C=0.32), and the resulting accuracy of the gaussian width and position is poor. We quantify the positional error by the distance between the fitted position $(x_1^{fit}, y_1^{fit})$ and the simulated position $(x_1^{sim}, y_1^{sim})$, normalized by the gaussian width $w_1$, or generally for a source $i$,

$$\frac{\Delta r_i}{w_i} = \frac{\sqrt{(x_i^{fit} - x_i^{sim})^2 + (y_i^{fit} - y_i^{sim})^2}}{w_i^{sim}} \ . \tag{29}$$

We quantify also the error of the fitted width by the normalized width,

$$\frac{\Delta w_i}{w_i} = \frac{(w_i^{fit} - w_i^{sim})}{w_i^{sim}} \ . \tag{30}$$

The positional error improves from $\Delta r_i/w_i \approx 1$ for sparse sampling down to $\Delta r_i/w_i \approx 0.01$ at the highest expected photon rates (Fig.6 top right panel); similarly for the width error (Fig.6 bottom right panel). Both errors scale roughly with the signal-to-noise ratio, i.e. $\Delta r_i/w_i \propto 1/\sqrt{R}$ and $\Delta w_i/w_i \propto 1/\sqrt{R}$. Note that the errors do not depend on the map pixel size used here (where the source is resolved, $w = 8"$, $\Delta x = 8"$), and drop to as low as 1% of the pixel size for high count rates. Therefore, subpixel accuracy is no surprise if the count rate is sufficiently high.

In Fig.7 we show a set of 100 simulations with single gaussian sources, having random positions $(-64" < x_1 < +64", -64" < y_1 < 64")$, random widths $(1" < w_1 < 20")$, and random photon rates $(3 < {}^{10}\log(R) < 5$, $R$ in units of cts$^{-1}$ SC$^{-1}$). The maps of all 100 simulations are shown in Fig.7, with the gaussian widths indicated. The positional errors, width errors, and flux errors are shown in the bottom diagrams of Fig.7. We find that the statistical errors for single gaussian fits can be characterized by

$$\frac{\Delta r_1}{w_1} = 10^{-1.27\pm0.46} \left(\frac{10^4\ cts/s/SC}{R}\right)^{1/2} = 0.05^{+0.10}_{-0.04} \left(\frac{10^4\ cts/s/SC}{R}\right)^{1/2} \tag{31}$$

$$\frac{\Delta w_1}{w_1} = 10^{-1.57\pm0.54} \left(\frac{10^4\ cts/s/SC}{R}\right)^{1/2} = 0.03^{+0.07}_{-0.02} \left(\frac{10^4\ cts/s/SC}{R}\right)^{1/2} \tag{32}$$

$$\frac{\Delta R}{R} = 10^{-1.92\pm0.43} \left(\frac{10^4\ cts/s/SC}{R}\right)^{1/2} = 0.012^{+0.020}_{-0.008} \left(\frac{10^4\ cts/s/SC}{R}\right)^{1/2} \tag{33}$$

Thus, for a count rate of $R = 10^4$ cts s$^{-1}$ SC$^{-1}$ and a single gaussian source (the simplest conceivable image), the typical error of the forward-fitting method is about 5% in position and about 3% in width (with respect to the gaussian source width), and about 1% in total flux. These statistics are based on 88 cases out of the 100 simulations shown in Fig.7, for sources that have a gaussian not smaller than half of the pixel resolution $(\Delta x = 8", w_1 > 4")$. In the other 12 cases with smaller sources (cases #2, 26, 29, 42, 45, 47, 51, 62, 67, 70, 74, 83, marked with grey numbers in Fig.7 bottom panels), the errors are systematically larger due to the under-resolution of the chosen pixel size, but can easily be corrected by repeating the forward-fitting with a smaller pixel size (on the expense of somewhat more computing time). Some other cases with large errors, e.g. cases #9, 49, 90, 31, 52, 75, 84, are clearly related to source positions near the edge of the chosen map boundaries. Those cases could also be improved by choosing a larger field-of-view.

### 5.3. Simulation of Double Sources

The forward-fitting of double sources involves 7 free parameters in the simplest parametrization (with 2 circular gaussians). We performed a number of simulation sequences of double sources with variations of individual parameters, such as the relative widths or amplitudes of the gaussian sources, the total photon flux, or the image resolution. In Figs.8 and 9 we show the results of a sequence of 100 simulations of double gaussian sources based on random parameters. The following random distributions have been used to simulate the 7 gaussian parameters of the 100 simulations: random logarithmic photon count rate $3 < {}^{10}\log(R) < 5$; random relative flux of the second source $0.1 < (f_2/f_1) < 1.0$; random gaussian widths in the range of 4" $< w_1 <$ 12", 4" $< w_2 <$ 12"; random source separation $(w_1 + w_2) < r_{sep} <$ 64" (with $r_{sep} = \sqrt{(x_1 - x_2)^2 + (y_1 - y_2)^2)}$); random orientation angle $0 < \varphi < 2\pi$ (with azimuth angle $\varphi = arctan[(y_2 - y_1)/(x_2 - x_1)]$); and random midpoint positions of the double source $-16" < x_0 < +16", -16" < y_0 < +16"$, with midpoints $x_0 = (x_1 + x_2)/2$ and $y_0 = (y_1 + y_2)/2$. The simulated maps together with the detailed values of the gaussian source widths $(w_1, w_2)$, the gaussian amplitude ratios $(a_2/a_1)$, and the relative flux ratios $f_2/f_1$ (where the relative flux ratio is proportional to the counts per gaussian source, i.e. $f_i \propto a_i \times r_i^2$), are shown in Fig.8.

We performed forward-fitting for all 100 simulations with a selected pixel size of 8" and a $16 \times 16$ map grid. (Remember that the code automatically adjusts the pixel size to a smaller field-of-view when the sources are found to be concentrated in an area that is smaller than the map.) The numerical code converged in all cases to a solution within a limit of $< 20$ iteration cycles. The positional errors $\Delta r_i/w_i$, width errors $\Delta w_i/w_i$, amplitude errors $\Delta a = a_2 - a_1$, and flux errors $\Delta R/R$, as measured from the difference of the forward-fitting solutions to the simulation models, are shown in Fig.9. It is useful to quantify the errors as function of the photon count rate per source,

$$R_1 = R\frac{f_1}{f_1 + f_2}\ , R_2 = R\frac{f_2}{f_1 + f_2}\ . \tag{34}$$

We show the positional and width errors separately for the two gaussian components in Fig.9, for the first gaussian in the top row of Fig.9 (as function of the source flux $R_1$), and for the second gaussian in the bottom row of Fig.9 (as function of $R_2$). We find a similar degree of accuracy in the positions and widths of double gaussians as for single gaussians (Section 5.1), except in cases with source confusion or weak secondary sources.

Source confusion occurs occurs when the separation distance $d$ between two gaussians (with amplitudes $a_1 = 1$, $a_2 < a_1$ and gaussian widths $w_1$, $w_2$ is smaller than the limit $w_{sep}$,

$$d \lesssim w_{sep} = w_1\sqrt{1 + \ln{(\frac{a_1}{a_2})}} + w_2\ . \tag{35}$$

We find 15 cases (# 6, 7, 15, 27, 32, 46, 55, 57, 62, 70, 76, 81, 82, 91, 95) with insufficient separation ($d \le w_{sep}$), which mostly exhibit larger errors in the forward-fitting of their positions and gaussian widths. In some cases our algorithm fails to resolve the two gaussians (# 27, 82), a limitation that is inherent to the initial source identification from the backprojection map.

Another difficulty is a large contrast between multiple sources. The weight of secondary sources in the $\chi^2$ or C-fit is essentially proportional to the number of photons contained in each gaussian component, i.e. their relative flux $R_i$ or $f_i \propto a_i \times w_i^2$. For gaussian components that have a small relative flux, say less than 5%, the forward-fitting procedure may not converge to the correct solution because of limited sensitivity. It may yield an alternative solution that is within the uncertainty of the data noise. Among the 100 simulations shown in Fig.8 there are 11 cases with a strong contrast of $f_2/f_1 < 0.05$, i.e. # 3, 5, 12, 17, 42, 53, 68, 77, 80, 87, 93. Our algorithm does not find a solution for the secondary gaussian for the cases #3, 12, 42, 77, and 87.

The results can be summarized as follows. Out of the 100 double-source simulations, a forward-fitting solution with two gaussians was found in 90 cases, using a fully automated computation mode without human interaction. For an uncontaminated statistics of errors we exclude cases with insufficient separation (35 cases with $d \le 1.5 \times w_{sep}$) and cases with weak secondary sources (11 cases with $f_2/f_1 < 0.05$), both subsets are indicated with grey numbers in Fig.9. From the remaining 55 cases we find the following statistical errors (Fig.9),

$$\frac{\Delta r_1}{w_1} = 10^{-0.96\pm0.42}(\frac{10^4\ cts/s/SC}{R})^{1/2} = 0.11^{+0.18}_{-0.07}(\frac{10^4\ cts/s/SC}{R})^{1/2} \tag{36}$$

$$\frac{\Delta r_2}{w_2} = 10^{-0.73\pm0.46}(\frac{10^4\ cts/s/SC}{R})^{1/2} = 0.19^{+0.35}_{-0.12}(\frac{10^4\ cts/s/SC}{R})^{1/2} \tag{37}$$

$$\frac{\Delta w_1}{w_1} = 10^{-1.28\pm0.55}(\frac{10^4\ cts/s/SC}{R})^{1/2} = 0.05^{+0.13}_{-0.04}(\frac{10^4\ cts/s/SC}{R})^{1/2} \tag{38}$$

$$\frac{\Delta w_2}{w_2} = 10^{-1.35\pm0.60}(\frac{10^4\ cts/s/SC}{R})^{1/2} = 0.04^{+0.13}_{-0.03}(\frac{10^4\ cts/s/SC}{R})^{1/2} \tag{39}$$

$$\Delta a = a_2 - a_1 = 10^{-1.14\pm0.50}(\frac{10^4\ cts/s/SC}{R})^{1/2} = 0.07^{+0.16}_{-0.05}(\frac{10^4\ cts/s/SC}{R})^{1/2} \tag{40}$$

$$\frac{\Delta R}{R} = 10^{-2.05\pm0.41}(\frac{10^4\ cts/s/SC}{R})^{1/2} = 0.009^{+0.013}_{-0.005}(\frac{10^4\ cts/s/SC}{R})^{1/2} \tag{41}$$

Thus, for a count rate of $R = 10^4$ cts s$^{-1}$ SC$^{-1}$ the two gaussian sources can be reconstructed with an automated forward-fitting method with a typical positional accuracy of $\approx 10-20\%$ and a width accuracy of $\approx 5\%$ (with respect to their gaussian width). The total photon flux is typically retrieved with an accuracy of $\approx 1\%$. Overlapping double sources or weak sources with a contrast of less than 1 : 20 are less reliably reconstructed.

### 5.4. Maximum Spatial Resolution

What is the spatial resolution of HESSI? The angular pitch of the finest grid #1 is $p_1 = 4.52$", which defines a FWHM resolution of $\alpha_1 = p_1/2 = 2.26$". For a gaussian source profile, the gaussian (half) width is $w = FWHM/(2 \times \sqrt{2 \ln 2}) = FWHM \times 0.42$, yielding a minimum gaussian width of $w_{res} = 0.95$". This high resolution can, however, only be achieved for sufficiently high photon statistics (see discussion in Section 4.2 and Fig.3). On the other side, the forward-fitting method is capable of "super-resolution" to some degree, down to a subpixel accuracy of $\approx 1\%$ as demonstrated in the simulations shown in Fig.6 (Section 5.1). To determine the maximum possible resolution of HESSI using the forward-fitting method we conduct a sequence of simulations with an unresolved source.

We set up a sequence of simulations with a single gaussian source at location ($x_1 = 2.5$", $y_1 = 2.5$") and a gaussian width of $w_1 = 0.1$" (i.e. $FWHM = 0.24$"). We vary the photon count rate from $R = 100, 300, 1000, ...$ to $10^5$ cts s$^{-1}$ SC$^{-1}$. We carry out the simulations with a resolutions of $\Delta x = 0.2$" (with a grid of $32 \times 32$, covering a field-of-view of $[-3.2", 3.2"]$). The results of the width measurements as function of the photon count rate $R$ are shown in Fig.10. The simulations demonstrate that super-resolution is achieved for count rates $R \gtrsim 1000$ cts s$^{-1}$ SC$^{-1}$, reaching an asymptotic value of $w_1^{fit} = 0.32 \pm 0.03$" ($FWHM = 0.76$"), which is a factor of $w^{res}/w_1^{fit} = 0.95"/0.32" = 3.0$ better than the nominal resolution. Thus, we can expect to resolve structures down to $FWHM \gtrsim 0.8$" (i.e. $\gtrsim 500$ km on the solar surface) with HESSI, using the forward-fitting method.

### 5.5. Convergence and C-statistic

The convergence behaviour of the forward-fitting algorithm provides an important criterion whether a solution is reached or not. The stopping criterion of a minimization algorithm is usually specified by a small limit of $\chi^2$ (or C-statistic) differences in subsequent iterations (here $\Delta C \le 10^{-4}$) or by a maximum number of iterations (here $n^{iter} \le 10$ for single gaussians, and $n^{iter} \le 20$ for double gaussian models). However, such stop criteria do not guarantee whether the best solution is reached. A test criterion is the final value of $\chi^2$ or the C-statistic, which is supposed to reach a value near unity if the best-fit reaches a model that is consistent with the data within the uncertainties of the expected data noise. In Fig.11 we show the distribution of the final C-statistic values for the 100 simulations with single gaussians (Fig.11 left second panel, Section 5.1) and for the 100 simulations with double gaussians (Fig.11 left forth panel, Section 5.2), which indeed have typical values in the range of $0.95 \lesssim C \lesssim 1.1$, as expected for good convergence behaviour. Values less than 1.0 could indicate that data noise is fitted, while values above 1.0 could indicate whether insufficient convergence occurred. Fortunately, simulations allow us to determine what the ideal C-value should look like for a particular case. This theoretical value can simply be obtained by calculating the $\chi^2$ or C-statistic by substitution of the best fit solution with the true solution specified by the simulation model. The corresponding distribution of the C-statistic are also shown in Fig.11 (left top and third panel). A comparison of the C-statistic from the true solutions (simulation model) and the best fits (by forward-fitting) will tell us whether the forward-fitting algorithm converged to the optimum value. This is shown in form of scatterplots in Fig.11 (right panels). Most of the C-values are identical for the simulations and the forward-fitting, indicating perfect convergence behaviour. For the 100 cases of single gaussians, some C-values of the best fit are slightly lower than the values expected from the true solution, indicating that the algorithm started to "fit the noise". For the case of double sources, a few cases show a slightly higher value of the C-statistic (in the range of $C \lesssim 1.2$), which indicates insufficient convergence. For the latter cases, a decrease of the limit $\Delta C \le 10^{-4}$ or an increase in the maximum limit of iterations is recommended. In the overall, the convergence behaviour of the forward-fitting code in the present implementation is quite satisfactory, given the consistent match of best-fit C-values and model-calculated C-values.

### 5.6. Uniqueness of Solutions

After we have gained confidence into the convergence performance of the forward-fitting code, we might also ask whether the solution found by the forward-fitting method is unique, or whether there are multiple solutions to the same data. The forward-fitting algorithm essentially solves the inversion of a 2-dimensional matrix $I_{ij}$ (the image) from a 4-dimensional matrix multiplication with $R_{ijkl}$ (the detector response matrix), yielding the 2-dimensional product $M_{kl}$ (the modulation time profiles). The question about the uniqueness of the inversion is equivalent to the problem whether two different matrices $I^1_{ij} \neq I^2_{ij}$ could exist that produce the same endproduct $M^1_{kl} = M^2_{kl}$, i.e.

$$\begin{aligned} M^1_{kl} &= R_{ijkl} \otimes I^1_{ij} \\ M^2_{kl} &= R_{ijkl} \otimes I^2_{ij} \ . \end{aligned} \tag{42}$$

This is equivalent to the equation of a non-trivial difference image $\Delta I_{ij} = I^1_{ij} - I^2_{ij} \neq \{0\}_{ij}$ that would produce a zero matrix $M^1_{kl} - M^2_{kl} = \{0\}_{kl}$,

$$(M^1_{kl} - M^2_{kl}) \equiv 0 = R_{ijkl} \otimes (I^1_{ij} - I^2_{ij}) = R_{ijkl} \otimes \Delta I_{ij} \ . \tag{43}$$

Thus, the question is about the existence of a non-trivial image $\Delta I_{ij} \neq \{0\}_{ij}$ that produces zero modulation $M_{kl}$. This question could formally be proven by checking analytically whether the matrix $R_{ijkl}$ satisfies the orthogonality condition. On the other hand, we can also answer the same question with a simple physical argument. There are indeed two particular situations that produce no modulation: (1) a photon incoming along the spin axis will not modulate the detector response, or (2) sources that have structures on a larger scale than the largest pitch (here 355") will not modulate the detectors either (yielding a flat time profile with a constant value). In those cases, the image $\Delta I_{ij}$ has not to be zero in all pixels $(i,j)$ but the modulation profile $M_{kl}$ will be zero or constant. The practical consequence is that any particular solution of an image $I_{ij}$ is non-unique plus or minus a constant background or a delta-function like peak at the phase center of the image. Besides these two special cases, every structure smaller than the pitch of the largest collimator necessarily produces a finite modulation profile, and thus consequently constitutes a unique solution of the inversion problem.

Empirical support for the uniqueness of the image solution is also warranted by the fact that all of our forward-fitting runs converged to a solution that is identical with the model simulation (within the uncertainties of the expected counting statistics).

### 5.7. Computation Time Considerations

The computation time of Fourier-type imaging algorithms is generally an issue of computational effort. Imaging with HESSI in particular, requires the calculation of modulation profiles which need to resolve the rotational modulation, and thus are by design much more computing intensive than non-rotating Fourier imagers. The computational effort mainly depends on 4 dimensions (spatial image $N_x \times N_y$, time profile $N_t$, and number of iterative (modulation profile) function calls $N_{iter}$), and thus the required computing time (or *Central Processing Unit (CPU)* time) of an image is roughly proportional to the product:

$$t^{CPU} = \Delta t^{machine} (N_x \times N_y \times N_t \times N_D \times N_{iter}) \tag{44}$$

where $\Delta t^{machine}$ is a machine-dependent multiplication time. The image dimensions depend on the required field-of-view and desired resolution (pixel size), which vary typically between $N_x \times N_y = 16 \times 16$ to $64 \times 64$ for HESSI (see discussion in Section 5.3). The number of time bins require to resolve the rotational modulation sum up to a total of $N_t = 17,792$ for all detectors #1-9, but can significantly be reduced by careful selection of detectors with significant counts, e.g. to $N_t = 1,408$ for detectors #6-9 (see discussion in Section 4.3). The number of iterations required to reconstruct an image strongly depends on the imaging algorithm, it amounts typically to $n_{iter} \approx 50$ to 250 (for 10-20 iteration cycles) for the forward-fitting technique performed here (Fig.12). To give an idea about typical computation times, we show the computation times of the 200 forward-fitting runs described in Sections 6.1 and 6.2, which took an average computation time of $t^{CPU} = 60 \pm 36$ s for single source models, and $t^{CPU} = 152 \pm 85$ s for double source models (performed on a *Silicon Graphics R5000 Indy* workstation). The same computations have been found to run about 3 times faster on other machines (e.g. on *IBM Thinkpad 600*, Pentium II processor, 266 MHz, 64 Mb RAM).

Although performance comparisons have not yet been carried out with other imaging algorithms, such as cleaning, maximum entropy method, polar mapping, pixon mapping, we expect that forward-fitting represents the most efficient way to reconstruct an image, because the image information to be fitted is reduced to a small number of free parameters (here $n^{free} = 3 - 7$ parameters for single and double gaussian sources), while the number of free degrees scales with the image size $N_x \times N_y$ in pixel-based imaging algorithms (such as cleaning or maximum entropy). An exception is the pixon method, which also reduces the equisized pixels $N_x \times N_y$ to larger non-equisized pixons, and thus has the potential to perform image reconstruction in a more efficient way. However, the disadvantage of the forward-fitting method is the requirement of simple source morphologies (that can adequately be represented by analytical functions), making it less general than other imaging methods.

## 6. SUMMARY AND CONCLUSIONS

We described a newly-developed forward-fitting method to reconstruct images from the *HESSI* telescope for simple source morphologies that can be represented by a superposition of multiple gaussians. We performed some 500 numerical simulations of HESSI telemetry files and compared the forward-fitted images with the model images in order to quantify the fidelity of the image reconstruction, the accuracy of the retrieved physical parameters, the maximum spatial resolution, the convergence behaviour, and the computational speed of the algorithm. These tests represent also a basic reference for all other *HESSI* image reconstruction algorithms, providing quantitative image accuracy criteria that are important for the scientific interpretation of HXR images anticipated from the HESSI solar flare mission (planned for launch in July 2000). The results of the forward-fitting method can be summarized as follows:

1. Using circular, elliptical, and curved gaussians, most of the so far observed HXR maps of solar flares can be represented by a relatively small number of free parameters, i.e. $n^{free} = 3$ for a single source, $n^{free} = 7$ for double sources, $n^{free} = 14$ for double footpoint flares with loop-top HXR emission, or $n^{free} = 18$ for Masuda-type flares. The current implementation of the forward-fitting code is designed to reconstruct HXR images for this variety of source morphologies. (The first two types are treated in this study, while the latter two types will be described in a subsequent Paper).

2. The minimum count rate required for a detector to produce significant modulation is approximately $R_l^{min} = 1000/\sqrt{3}^{(i-1)}$ cts s$^{-1}$ SC$^{-1}$ for detector $l = 1, ..., 9$, i.e. $R_1^{min} \approx 1000$ cts s$^{-1}$ SC$^{-1}$ for the finest detector #1, and $R_9^{min} \approx 10$ cts s$^{-1}$ SC$^{-1}$ for the coarsest detector #9. For a given flare event with count rate $R$, detectors that have a count rate below this limit, $R_l^{min} < R$, can be discarded for image reconstruction without loss of any significant information. This saves considerable computational effort.

3. Test runs of forward-fitting with model maps containing a single gaussian source show that the relative accuracy of most gaussian parameters scales with the signal-to-noise ratio, i.e. $\propto \sqrt{R}$, with $R$ being the photon count rate. The average accuracy in the reconstruction of single gaussian sources at a count rate of $R = 10^4$ cts s$^{-1}$ SC$^{-1}$ is $\approx 5\%$ for the position and $\approx 3\%$ for the gaussian source width, both with respect to the gaussian source width. The accuracy depends primarily on the photon count rate and not at all on the chosen pixel size (as long as the source is larger than the half pixel size). Subpixel accuracies down to 1% can be achieved for count rates of $R \approx 10^5$ cts s$^{-1}$ SC$^{-1}$. This allows to perform efficient mapping with relative large pixel sizes without losing accuracy.

4. Test runs of forward-fitting with model maps containing double gaussian sources demonstrate that the positions and widths can be reconstructed with almost the same accuracy as single source maps, unless there are source confusion problems or strong contrast ( $\lesssim 1:20$ for the weaker source). However, we find that the forward-fitting code converges to a $\chi^2$ or C-statistic value that is equally consistent with the data as the model. The resulting differences thus represent an ambiguity in the

mathematical parametrization of a map within the uncertainties of the photon count statistics rather than a numerical image reconstruction problem.

5. The maximum spatial resolution that can be obtained with the forward-fitting technique is $\mathrm{FWHM}^{min} \approx 0.8$", which is about a factor of 3 below the nominal resolution of the finest grid, i.e. $\mathrm{FWHM}_1^{res} = 2.3$".

6. We find that the forward-fitting algorithm virtually always converges to the same solution as the model (used for the simulation of the telemetry data), based on the experience from some 500 different simulations. The final $\chi^2$- and C-statistic values reached at the convergence limit, which are found in the range of $0.95 \lesssim C \lesssim 1.1$, are constrained by the noise statistics of a particular event, and not by the convergence behaviour of the forward-fitting code.

7. We find no evidence for multiple image solutions to a given observed modulation time profile, neither on mathematical nor on numerical grounds. The image solution obtained by forward-fitting in $n^{free}$-dimensional parameter space seems to represent a unique solution (within the uncertainties of the count statistics).

Future work with the forward-fitting method will include (1) the simulation of HESSI telemetry data with more complex source morphologies (i.e. curved loops, Masuda-type flares), (2) combined spatial-spectral imaging, (3) combined spatial-temporal imaging, (4) fast imaging on time intervals shorter than a half spacecraft spin period, and quantitative comparisons with other HESSI imaging methods.

*Acknowledgements:* Support for this work was provided by the NASA SMEX grant NAS-..... through UCB (subcontract SA2241-26308PG).

## A. APPENDIX: $\chi^2$ and C-statistic for Sparse Sampling

An observed time series of photon counts, $f^{obs}(t)$, which is binned into time intervals of length $\Delta t$, so that the number $n_i = f^{obs}[t_i < t < t_i + \Delta t]$ represents the photon counts in bin $[t_i, t_i + \Delta t]$, is modeled by an analytical function, $f^{model}(t)$, which predicts an expectation value $e_i = f^{model}[t_i < t < t_i + \Delta t]$ of photon counts in time bin $i$. In the limit of large-number counts, $n_i \gg 0$, Poisson statistics can be approximated by a gaussian distribution, which predicts an r.m.s. noise of $\sigma_i = \sqrt{e_i} \approx \sqrt{n_i}$. The goodness of fit of a model can then be evaluated by the well-known $\chi^2$-statistic,

$$\chi^2 = \frac{1}{N} \sum_{i=1}^{N} \frac{(n_i - e_i)^2}{\sigma_i^2} = \frac{1}{N} \sum_{i=1}^{N} \frac{(n_i - e_i)^2}{e_i} \ , \qquad \text{(A1)}$$

yielding a normalized value of $\chi^2 \approx 1$ in the case when the model is consistent with the data, within the uncertainties of the expected noise.

For sparse sampling, in particular when the observed time series $n_i$ contains zero's or few counts, say $n_i \lesssim 10$, e.g. as it is the case for the modulation patterns of the finest HESSI collimators, where the total photon counts are binned into some $2^{12} = 4096$ time bins to resolve the rotational modulation, the gaussian $\chi^2$-statistic is not appropriate anymore. Photon counting statistics for sparse sampling can be derived from the general probability function $P$ as outlined by Cash (1979), which is

$$P = \prod_{i=1}^{N} \frac{e_i^{n_i} e^{-e_i}}{n_i!} \tag{A2}$$

for a particular result $n_i$ given the correct set of $e_i$. The likelihood ratio, called *C-statistic* by Cash (1979), can be expressed in logarithmic form from Eq.A2,

$$C_{Cash} = -2 \ln P = -2 \sum_{i=1}^{N} (n_i \ln e_i - e_i - \ln n_i!) \ . \tag{A3}$$

Let the theoretical model $e_i(\Theta_1, ..., \Theta_p)$ be defined by $p$ free parameters $\Theta_i, i = 1, ..., p$. The best-fitting model is found by varying all $p$ parameters $\Theta_1, ..., \Theta_p$ until the C-statistic reaches a minimum, which we denote by $(C_{min})_p$. Now, during the iterative fitting procedure, only a partial subset of model parameters, say $q$ parameters (with $q < p$), may have already converged to the true solution, $\Theta_1^T, ..., \Theta_p^T$, so that $\Theta_1, ..., \Theta_q$ are set to $\Theta_1^T, ..., \Theta_q^T$, while the remaining $p - q$ parameters, $\Theta_{q+1}, ..., \Theta_p$, still need to be varied until a global minimum of $C$ is reached. We denote this partial solution, where $p - q$ parameters have already converged to the true solution $\Theta_i^T$, with the value $(C_{min})_{p-q}^T$. According to the theorem of Wilks (1938; 1963), the difference,

$$\Delta C = (C_{min})_{p-q}^T - (C_{min})_p \tag{A4}$$

will be distributed as $\chi^2$ with $q$ degrees of freedom. Therefore, the quantity $\Delta C$ can be used to establish a confidence criterion of the model $e_i$ to the data $n_i$. Following Cash (1979), the term $\ln(n_i!)$ of Eq.A3 drops out in the difference $\Delta C$, because only the parameters $e_i(\Theta_1, ..., \Theta_p)$ are varied during the fitting procedure. Thus, it is more convenient to use the simplified statistic

$$C_{simplified} = -2 \ln P = -2 \sum_{i=1}^{N} (n_i \ln e_i - e_i) \ . \tag{A5}$$

For the evaluation of the difference $\Delta C$ in Eq.A4 we have the partially optimized term $(C_{min})_{p-q}^T$,

$$(C_{min})_{p-q}^T = -2 \sum_{i=1}^{N} (n_i \ln{(e_i)_{p-q}^T} - (e_i)_{p-q}^T) \ , \tag{A6}$$

and the absolute minimum $(C_{min})_p$, which represents the asymptotic limit when the data $n_i$ perfectly match the model, i.e. $e_i = n_i$,

$$(C_{min})_p = -2 \sum_{i=1}^{N} [n_i \ln(n_i) - n_i] \ . \tag{A7}$$

The combination of Eq.A4-A6 yields then

$$\Delta C = -2 \sum_{i=1}^{N} [n_i \ln(e_i) - e_i - n_i \ln(n_i) + n_i] \ . \tag{A8}$$

Instead of the reduced $\chi^2$-statistic (A1), we can therefore use the equally-simple C-statistic (where we drop the symbol $\Delta$ for brevity),

$$C := \frac{1}{N} \Delta C = \frac{2}{N} \sum_{i=1}^{N} [n_i \ln(\frac{n_i}{e_i}) - (n_i - e_i)] \ . \tag{A9}$$

This form has the advantage that, in addition to being asymptotic to $\chi^2$, C vanishes identically when the model fits the data exactly. Numerical care has to be taken for the time bins that contain zeros in the data, $n_i = 0$, in which case the mathematical relation $n_i \ln(n_i) = 0$ has to be used to avoid the singularity $\ln(n_i) \mapsto \infty$. On the other side, a singularity could arise when the model predicts zero counts, $e_i = 0$, but the observed counts are not zero, $n_i \neq 0$, because the term $-n_i \ln(e_i)$ yields than infinity. It seems therefore to be recommendable to restrict the model fit to time intervals with a finite probability for photon counts, i.e. $e_i > 0$.

## References

Bevington,P.R. 1969, Data Reduction and Error Analysis for the Physical Sciences, New York: McGraw-Hill Book Company

Cash,W. 1979, ApJ 228, 939

Cornwell,T.J. and Evans,K.F. 1985, AA 143, 77

Crannell,C.J. 1988, in MAX'91 Workshop on "Flare Research at the Next Solar Maximum", (eds. R.C.Canfield and B.R.Dennis), p.164

Crannell,C.J., Hurford,G.J., Orwig,L.E., and Prince,T.A. 1986, SPIE 571, 142.

Crannell,C.J. et al. 1994, American Institute of Aeronautics and Astronautics: Washington DC., AIAA-94-0299.

Csillaghy,A. 1999, HESSI Data Analysis Meeting, Oct 22, NASA/GSFC, Greenbelt, MD

Dennis,B.R. 1994, Symp. on New Look at the Sun with Emphasis on Advanced Observations of Coronal Dynamics and Flares, Kofu, Japan, (eds. S.Enome and T.Hirayama), Nobeyama Radio Observatory, Report No.360, p.313

Dennis,B.R. et al. 1996a, SPIE 2804, 228

Dennis,B.R. et al. 1988, in MAX'91 Workshop on "Flare Research at the Next Solar Maximum", (eds. R.C.Canfield and B.R.Dennis), p.153

Dennis,B.R. et al. 1996b, AAS Meeting 188, #70.16

Enome,S. 1982, Adv.Space Res. 2/11, 201

Freeland,S.L. and Handy,B.N. 1998, Solar.Phys. 182, 497

Gaither III.,C.C., Schmahl,E.J., Crannell,C.J., Dennis,B.R., Lang,F.L., Orwig,L.E., Hartman,C.N., and Hurford,G.J. 1996, Appl.Optics 35, 6714

Gull,S.F. and Daniell,G.J. 1978, Nature 272, 686

Hogbom,J.A. 1974, AASS 15, 417

Hurford,G.J. 1992, in The Sun, A Laboratory for Astrophysics, Proc. of NATO workshop, (eds. J.T.Schmelz and J.C.Brown), Kluwer Academic Publishers

Hurford,G.J. 1997, AAS SPD Meeting 29, #13.02

Hurford,G.J. 1999a, AAS Meeting 194, #80.01

Hurford,G.J. 1999b, HESSI Data Analysis Meeting, Oct 22, NASA/GSFC, Greenbelt, MD

Hurford,G.J. 2000, "HESSI Imaging and Data Analysis", in "High Energy Solar Physics Workshop: Anticipating HESSI", (eds. R.Ramaty and Mandzhavidze,N.), APS, in press

Hurford,G.J. et al. 2000, "The Imaging Capabilities of HESSI", in preparation

Kosugi,T., Sawa,M., Sakao,T., Masuda,S., Inda-Koide,M., Yaji,K., and Sato,J. 1995, The Yohkoh HXT databook October 1991 - December 1994, Natl.Astron.Obs. Tokyo, Japan

Kraus,J.D. 1966, Radio Astronomy, McGraw-Hill, Cygnus-Quasar Books

Lin,P.R., Dennis,B.R., Emslie,A.G., Ramaty,R., Canfield,R., and Doschek,G. 1993, Adv.Space Res. 13/9, 401

Lin,P.R., Dennis,B.R., Ramaty,R., Emslie,A.G., Canfield,R., and Doschek,G. 1994, Geophysical Monograph 84, Washington DC:AGU, 283

Lin,P.R. et al. 1998, SPIE 3442, p.2

Makishima,K., Miyamoto,S., Murakami,T., Nishimura,J., Oda,M., Ogawara,Y., and Tawara,Y. 1977, in New Instrumentation for Space Astronomy, (K.A. van der Hucht and G.Vaiana eds.), New York: Pergamon Press

Masuda,S., Kosugi,T., Hara,H., Tsuneta,S., and Ogawara,Y. 1994, Nature 371, No. 6497, 495

McTiernan,J. 1999, HESSI Data Analysis Meeting, Oct 22, NASA/GSFC, Greenbelt, MD

Mertz,L.N., Nakano,G.H., and Kilner,J.R. 1986, J. Opt. Soc. Am. 3, 2167

Metcalf,T.R. 1999, HESSI Data Analysis Meeting, Oct 22, NASA/GSFC, Greenbelt, MD

Ohki,K., Tsuneta,S., Takakura,T., Nitta,N., Makishima,K., Murakami,T., Ogawara,Y., Oda,M., Miyamoto,S. 1982, Proc. Hinotori Symp. on Solar Flares, ISAS, Tokyo, Japan, p. ...

Orwig,L.E. et al. 1989, Max 91 Workshop 2: Developments in Observations and Theory for Solar Cycle 22, p.143

Press,,W.H., Flannery,B.P., Teukolsky,S.A., and Vetterling,W.T. 1986, Numerical Recipes, The Art of Scientific Computing, Cambridge: Cambridge University Press

Prince,T.A., Hurford,G.J., Hudson,H.S., and Crannell,C.J. 1988, Solar Phys. 118, 269

Rohlfs,K. 1986, Tools of Radio Astronomy, Berlin: Springer

Sakao,T. 1994, PhD. Thesis, University of Tokyo

Sato,J., Sawa,M., Masuda,S., Sakao,T., Kosugi,T., and Sekiguchi,H. 1998, The Yohkoh HXT Image Catalogue, October 1991-August 1998, Nobeyama Radio Observatory/NAO, Japan

Schmahl,E.J., and Dennis,B.R. 1993, AAS Meeting 183, #08.06

Schmahl,E.J., and Dennis,B.R. 1997, AAS, SPD Meeting 29, #02.14

Schmahl,E.J. 1999a, AAS Meeting 194, #77.02

Schmahl,E.J. 1999b, HESSI Data Analysis Meeting, Oct 22, NASA/GSFC, Greenbelt, MD

Schwartz,R.A. 1999, HESSI Data Analysis Meeting, Oct 22, NASA/GSFC, Greenbelt, MD

Smith,D. 1999, HESSI Data Analysis Meeting, Oct 22, NASA/GSFC, Greenbelt, MD

Smith,D. 2000, "HESSI Spectroscopy", in "High Energy Solar Physics Workshop: Anticipating HESSI", (eds. R.Ramaty and Mandzhavidze,N.), APS, in press

Takakura,T. et al. 1983, in Hinotori Symp. on Solar Flares, ISAS, Tokyo, Japan

Tsuneta,S. 1984, Tokyo University, Tokyo Astronomical Observatory, Annals, Second Series, 20, p.1

Wilks,S.S. 1938, Ann.Math.Stat. 9, 60

Wilks,S.S. 1963, Mathematical Statistics (Princeton: Princeton University Press), Chap.13

Table 1. HESSI Data Structure

| Detector # $l$ | Angular pitch (") $\alpha_l^{pitch}$ | FWHM resolution (") $\alpha_l^{res}$ | Modulation per rotation $N_l^{mod}$ | Data time bins $N_l^{bin}$ | Time bin $\Delta t_l$ (ms) | Minimum count rate $R_l^{min}(s^{-1}SC^{-1})$ |
|---|---|---|---|---|---|---|
| 1 | 4.52" | 2.26" | 6470 | $2^{13} = 8192$ | 0.512 | 900 |
| 2 | 7.84" | 3.92" | 3735 | $2^{12} = 4096$ | 1.024 | 450 |
| 3 | 13.57" | 6.79" | 2157 | $2^{11} = 2048$ | 2.048 | 220 |
| 4 | 23.5" | 11.8" | 1245 | $2^{10} = 1024$ | 4.096 | 110 |
| 5 | 40.7" | 20.4" | 719 | $2^{10} = 1024$ | 4.096 | 110 |
| 6 | 70.5" | 35.3" | 415 | $2^{9} = 512$ | 8.192 | 54 |
| 7 | 122.2" | 61.1" | 240 | $2^{9} = 512$ | 8.192 | 72 |
| 8 | 211.6" | 105.8" | 138 | $2^{8} = 256$ | 16.384 | 38 |
| 9 | 366.5" | 183.2" | 80 | $2^{7} = 128$ | 32.768 | 17 |

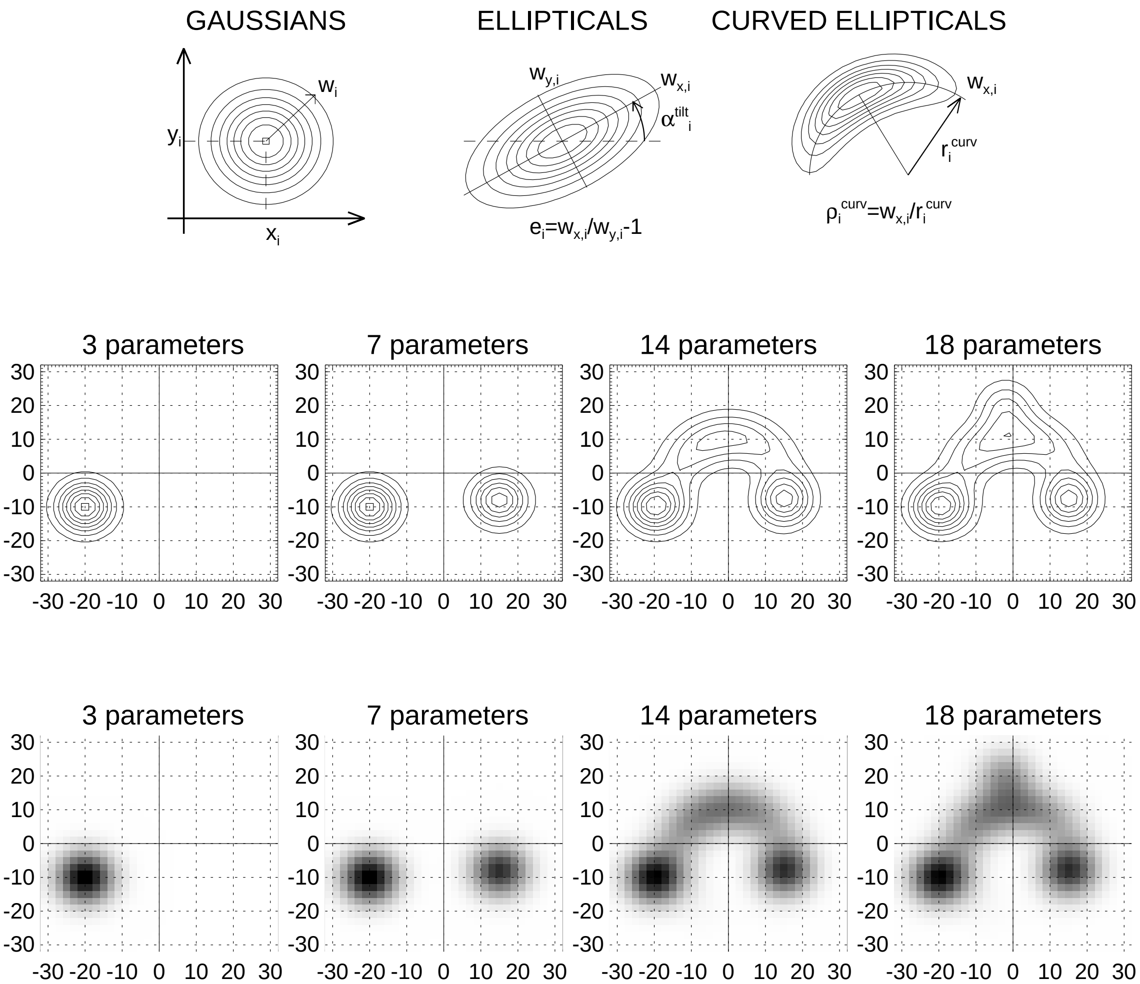


Fig. 1.— The parametrization of model maps, using circular gaussians (4 parameters, $x_i, y_i, w_i, f_i$), elliptical gaussians (6 parameters, plus $e_i, \alpha_i^{tilt}$), and curved ellipticals (7 parameters, plus $\rho_i^{curv}$), are defined in the upper panels. The middle and lower row show 4 examples with superpositions of the basic geometric elements defined above, characterized by 1,2,3 and 4 elements, specified by 3,7,14, and 18 free parameters. The parameters are: left footpoint ($f_1 = 1, w_1 = 5", x_1 = -20", y_1 = -10"$), right footpoint ($f_2 = 0.8, w_2 = 5", x_2 = +15", y_2 = -8"$), loop source ($f_3 = 0.6, w_3 = 15", x_3 = -2", y_3 = +10", e_3 = 2, \alpha_3^{tilt} = 10^0, \rho_3^{curv} = 1$), and above-the-looptop source ($f_4 = 0.4, w_4 = 5", x_4 = -2", y_4 = 20"$).

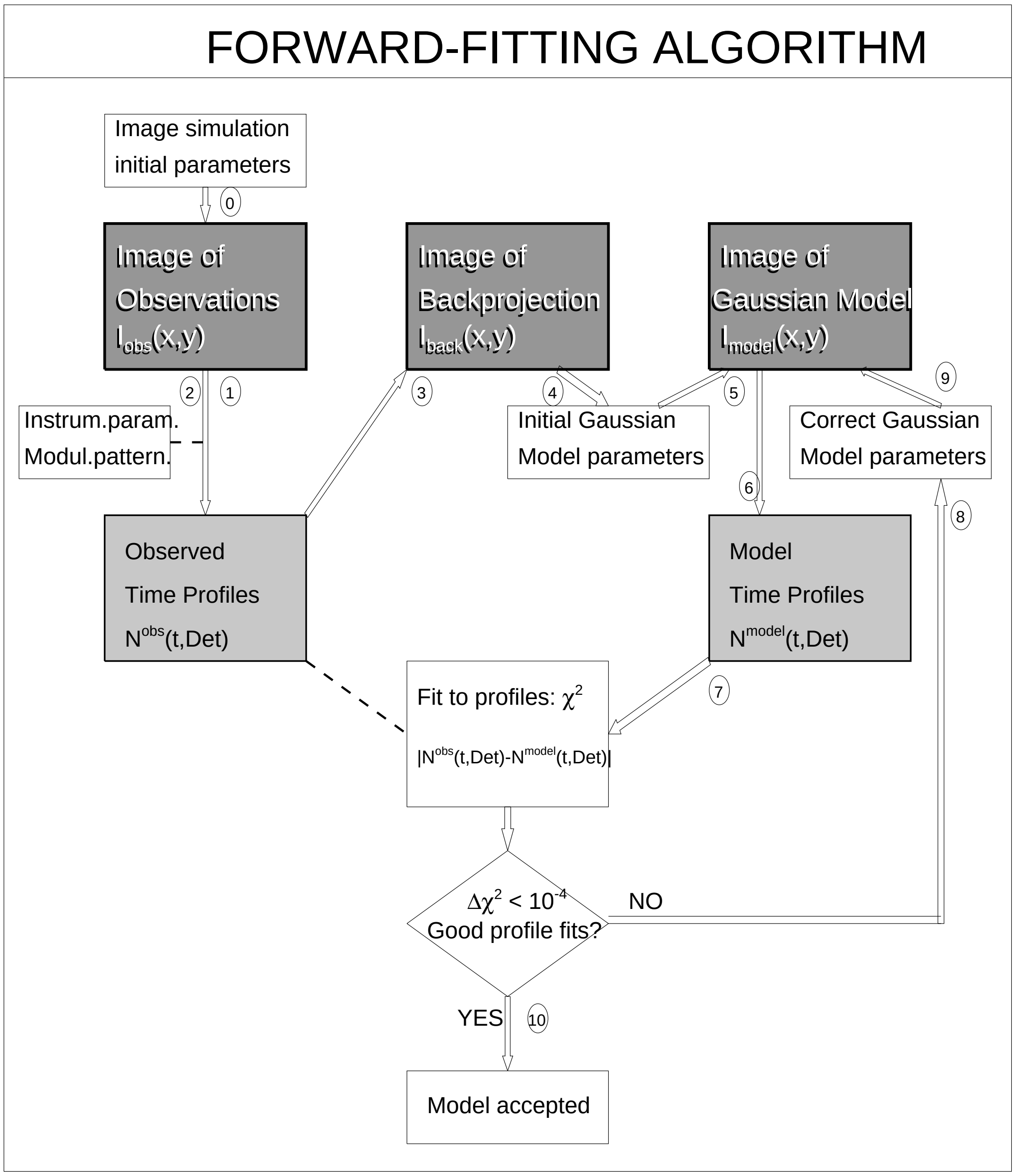


Fig. 2.— Flow chart of the numeric algorithm of forward fitting (see description of 10 basic steps in Section 5.1).

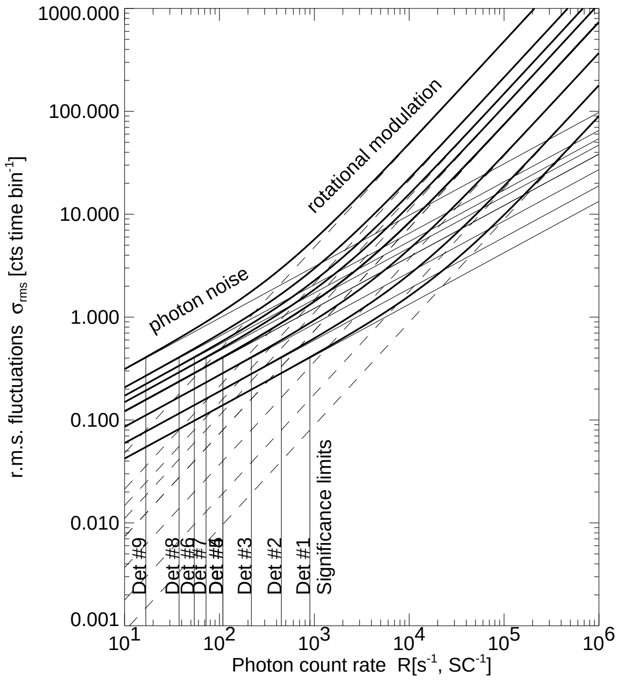


Fig. 3.— Thr r.m.s. fluctuations of observed time profiles $N^{obs}(t_k, D_l)$ as function of the photon count rate $R$ (thick lines), modeled in terms of two components: the photon counting r.m.s. noise $\sigma^{noise} \propto \sqrt{R}$ (thin lines), and the r.m.s. fluctuations due to the rotational modulation $\sigma^{mod} \propto R$ (dashed lines). Each component is shown for each detector $l$, $D_1, ..., D_9$, where the coarsest detector $D_9$ represents the topmost lines. Note that the photon noise dominates for small photon count rates $R_l$. The limit $R_l^{min}$ where the rotational modulation exceeds 20% of the photon noise is indicated with a vertical line for each detector. These values of $R_l^{min}$, which represent lower limits for the photon rate where rotational modulation is detectable in time profiles, are also listed in Table 2.

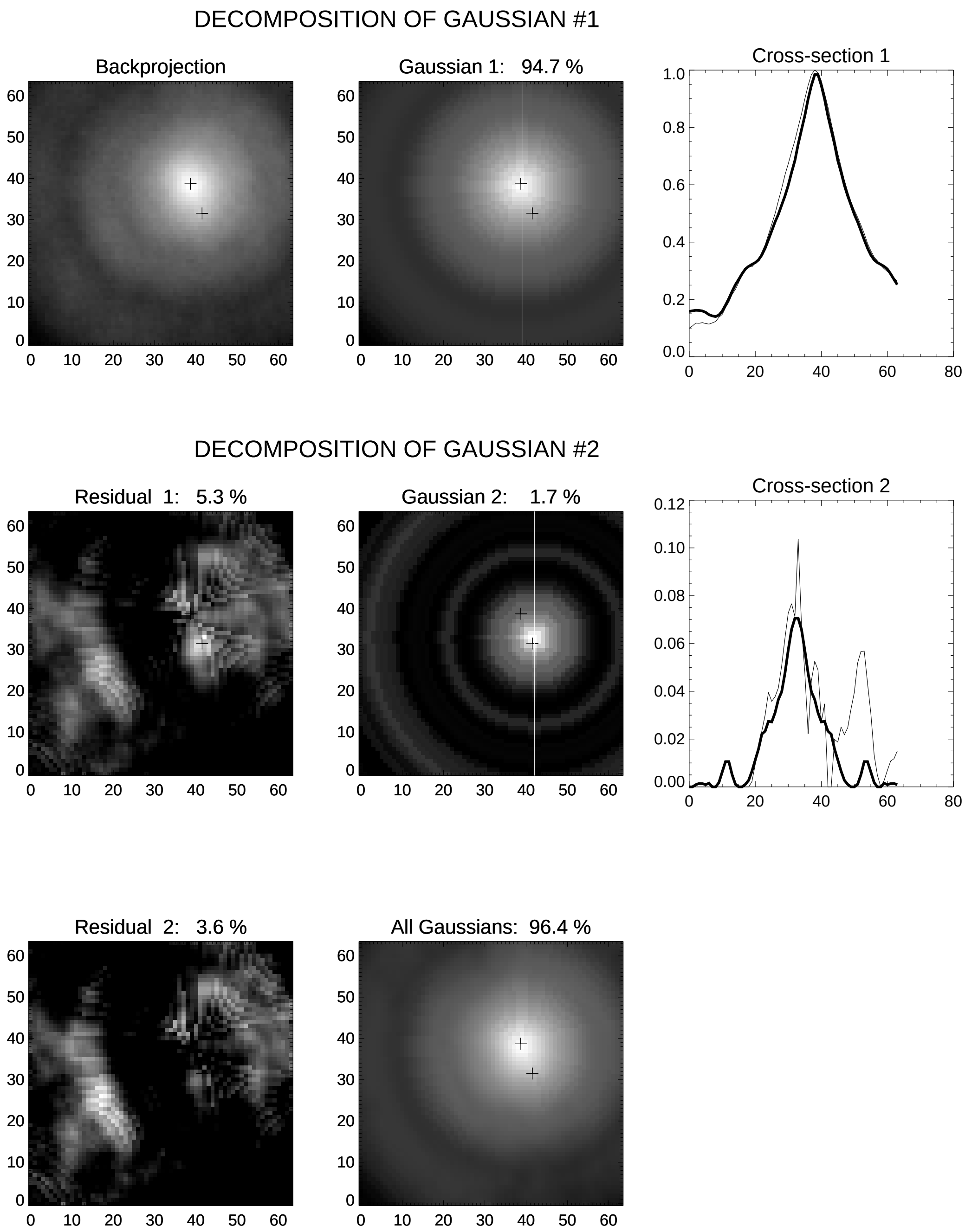


Fig. 4.— Decomposition of gaussian source components from a backprojection map. The original backprojection map is shown top left, the subtraction of 2 gaussian components is shown in the middle column, and the residuals in the left column. The map cross-sections along a vertical line through the source maxima (indicated with a white line in the middle column) are shown in the right column (thin line = original or residual map; thick line = subtracted source with circular rings).

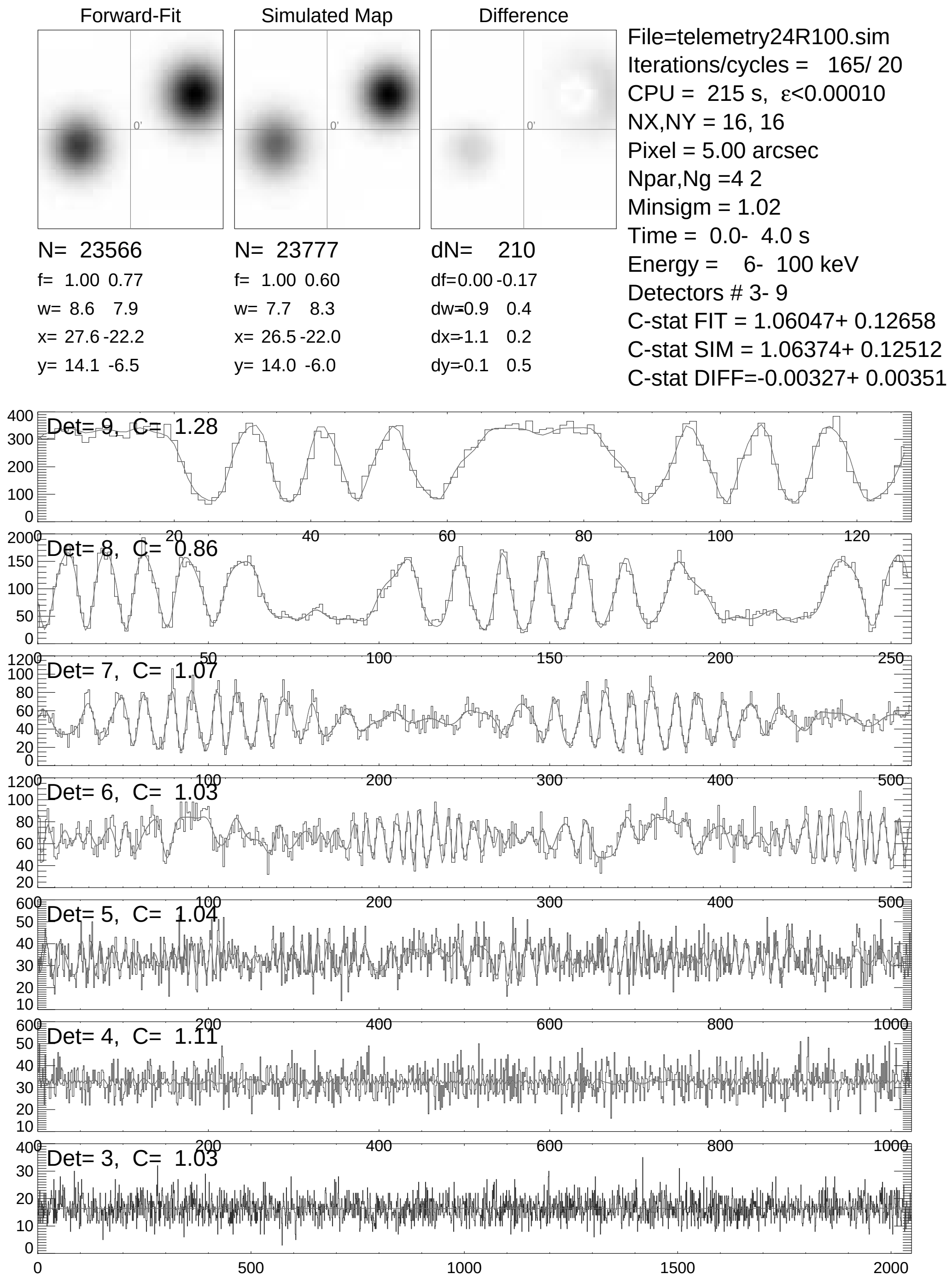


Fig. 5.— An example of a data set is shown, consisting of 7 time profiles from detectors #3-9 (histogrammed curves). The best-fits to the time profiles are shown as black curves and the expected time profiles from the model are plotted in gray (not visible here because the best-fit lies exatly on top of it. The resulting map from the forward-fit is shown in the top left panel, the model map in the middle panel, and the difference map on the right panel (with black indicating the absolute value of the difference).

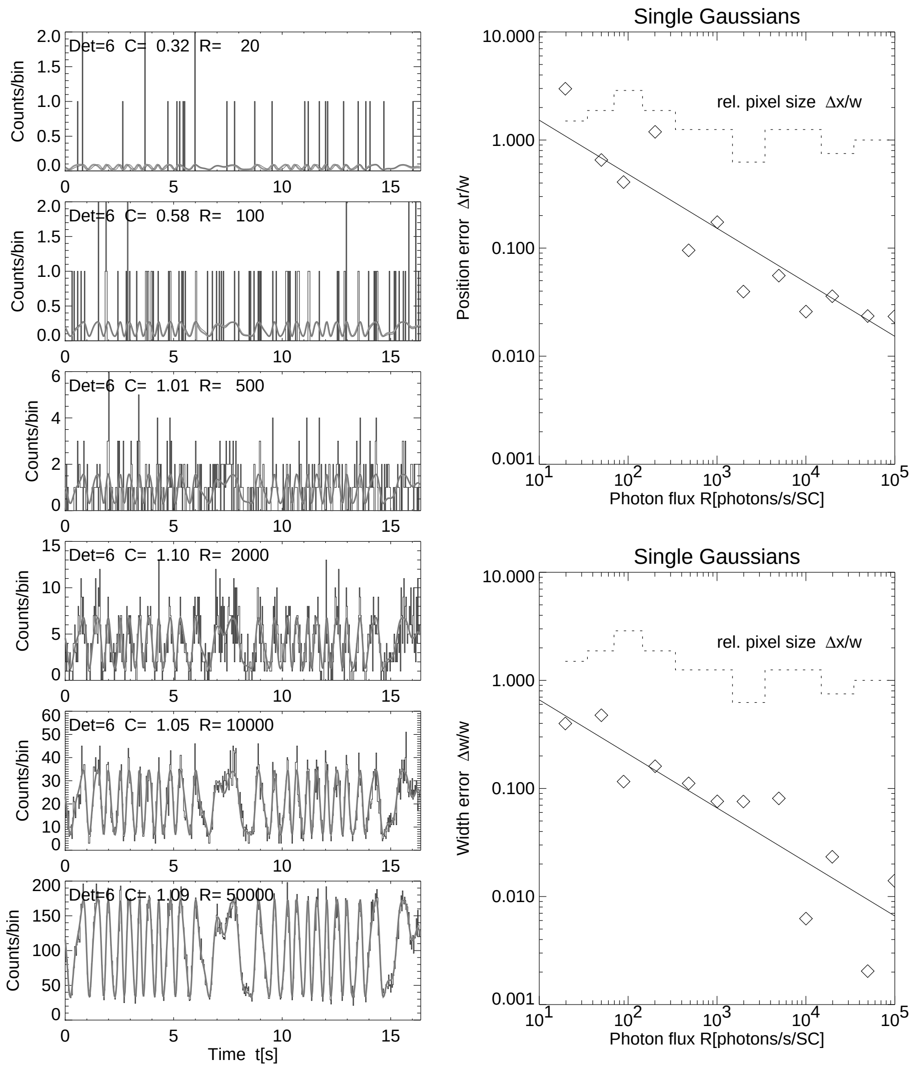


Fig. 6.— Simulations of single gaussian sources with varying photon flux rate from $R = 10$ to $R = 10^5$ cts$^{-1}$ SC$^{-1}$. The fit to the time profiles $N(t_k, D_l)$ are shown for detector #6 for 6 different simulations (left panels). The relative errors of the fitted position, $\Delta r/w$ (right top panel), and of the fitted gaussian width, $\Delta w/w$ (right bottom panel), are shown for a set of 12 simulations. The pixel width is also indicated (dotted). The gaussian width is always $w = 8$". Note that the errors drop down to $\approx 1\%$ of the pixel size for high count rates. The solid line in the right panels represents the best fit of a function that corresponds to the theoretical signal-to-noise ratio, $\propto \sqrt{R}$.

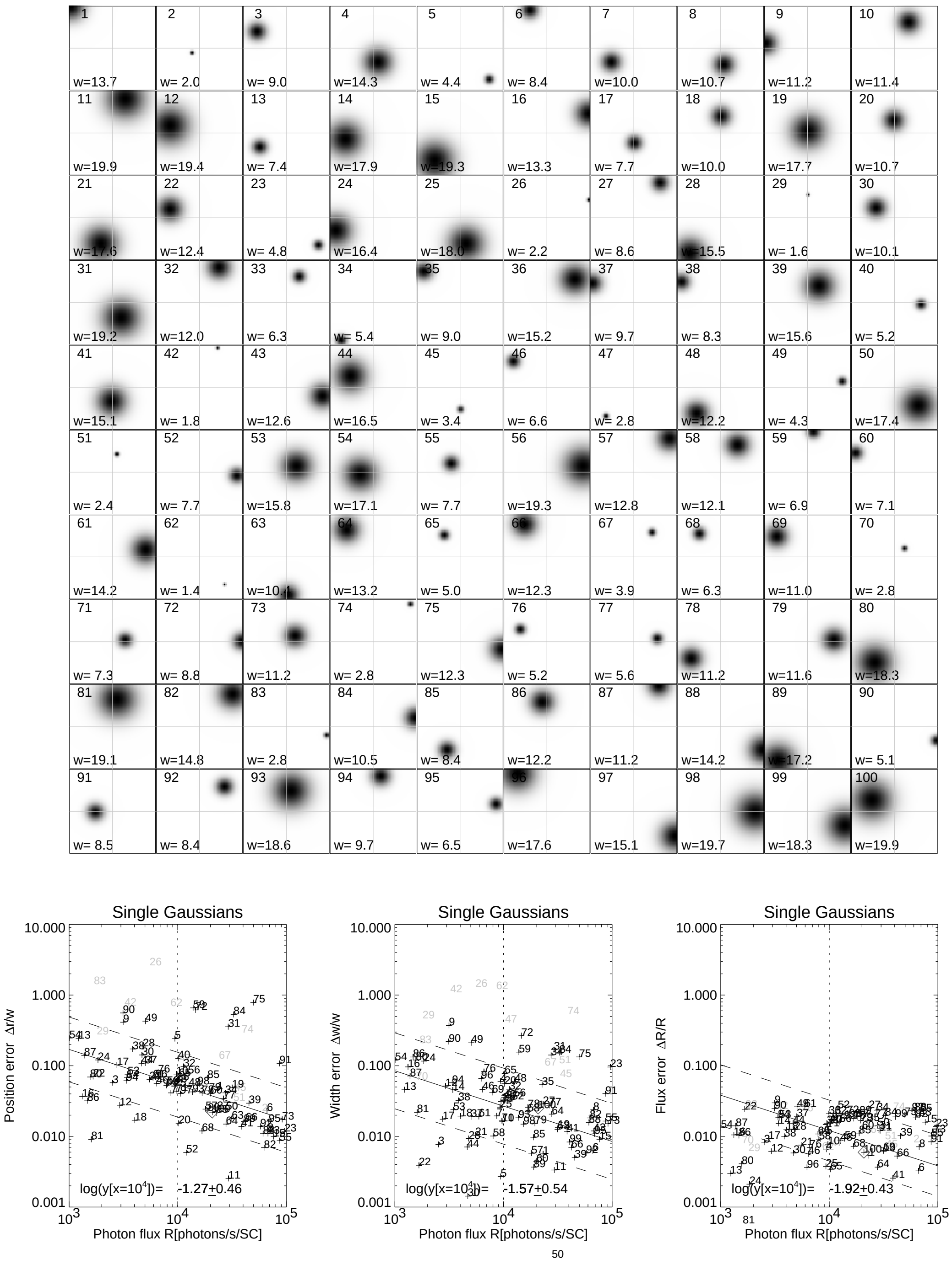


Fig. 7.— 100 simulations of single gaussian sources with random positions, random widths (indicated with symbol $w$ in each frame in arcseconds), and with random fluxes. The errors (i.e. normalized differences of the fitted to the simulated values) are shown in the bottom diagrams, with the map number indicated. The mean (solid line) and standard deviations (dashed lines) of the errors is fitted with a relation proportional to the signal-to-noise ratio $\propto \sqrt{R}$. The grey numbers refer to cases with sources located near the map boundaries and are not included in the statistic.

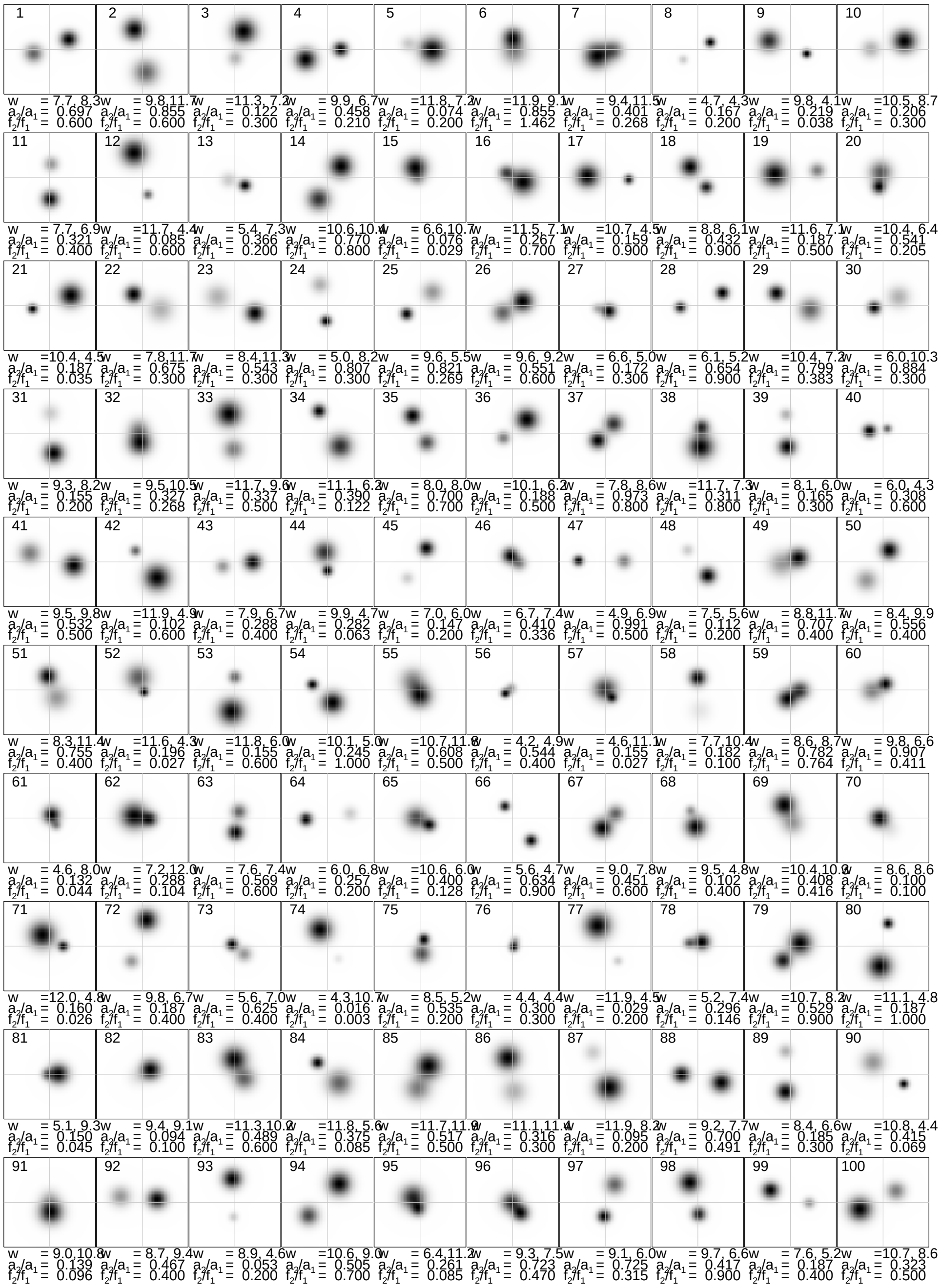

Fig. 8.— 100 simulations of double gaussian sources with random distances, orientations, gaussian widths, relative fluxes, and total fluxes (see specifications in Section 5.2). The intensity of the maps is shown here normalized to unity (black). The individual values of the two gaussian widths ($w$) (in arcseconds), the flux amplitude ratio ($a_2/a_1$), and the photon count ratio per source, $f_2/f_1 = (a_2 \times r_2^2)/(a_1 \times r_1^2)$ are indicated for each case. The numbering of the cases from 1 to 100 is used in the diagrams in Fig.9.

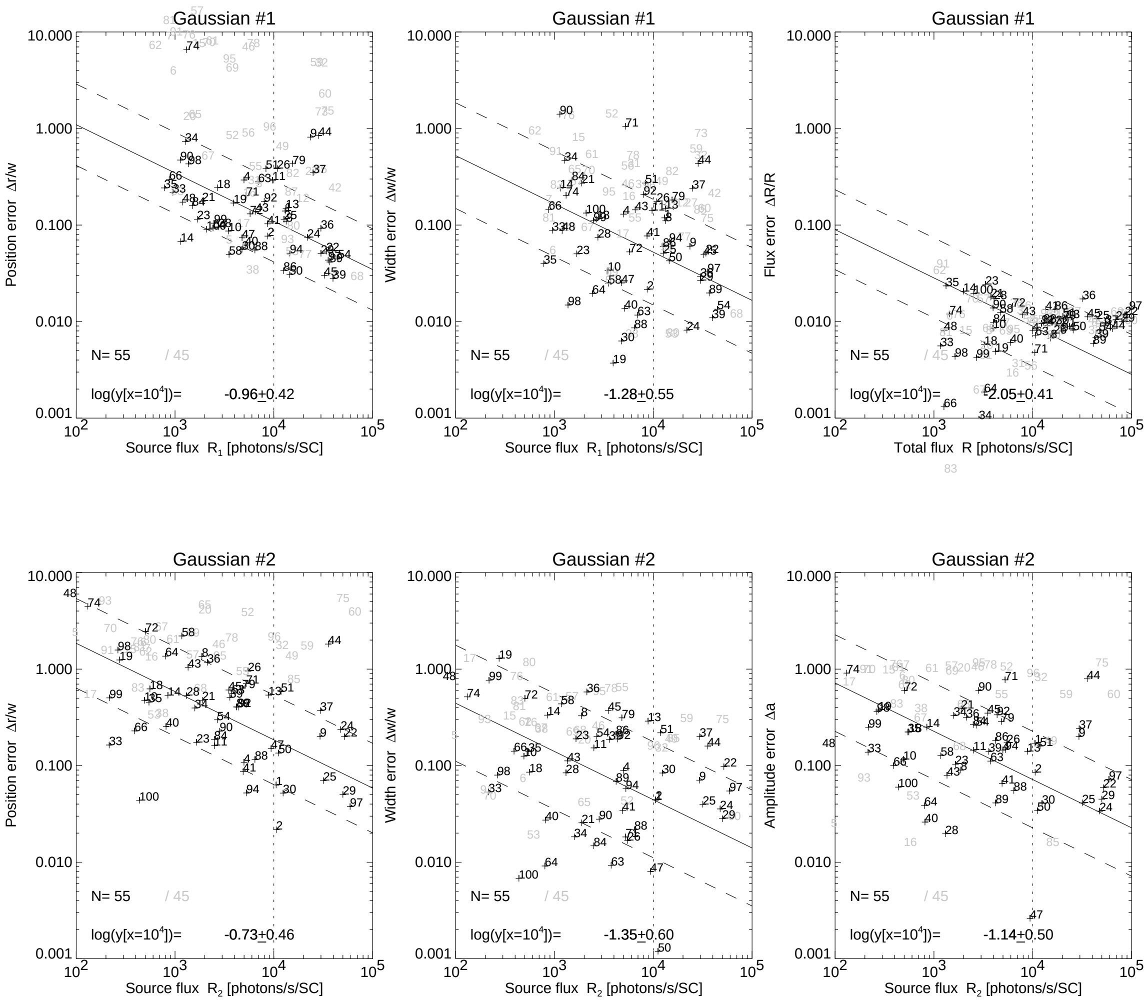


Fig. 9.— The differences between the source positions $r$, gaussian widths $w$, flux amplitudes $a$, and total photon flux $R$ of the model simulations and the forward-fitting solutions are quantified in normalized units, separately shown for the primary gaussian (top panels) and the secondary weaker gaussian (bottom panels). The grey numbers indicate cases with confusion problems ($d \le 1.5 w_{sep}$) or strong contrast problems $f_2/f_1 \le 0.05$, while the black numbers refer to cases without these problems. The errors of the latter group is quantified by the logarithmic mean and standard deviation ($log(y[x = 10^4])$, scaled by a flux-dependent signal-to-noise ratio, i.e. with the factor ($R/10^4$ cts$^{-1}$ SC$^{-1}$).

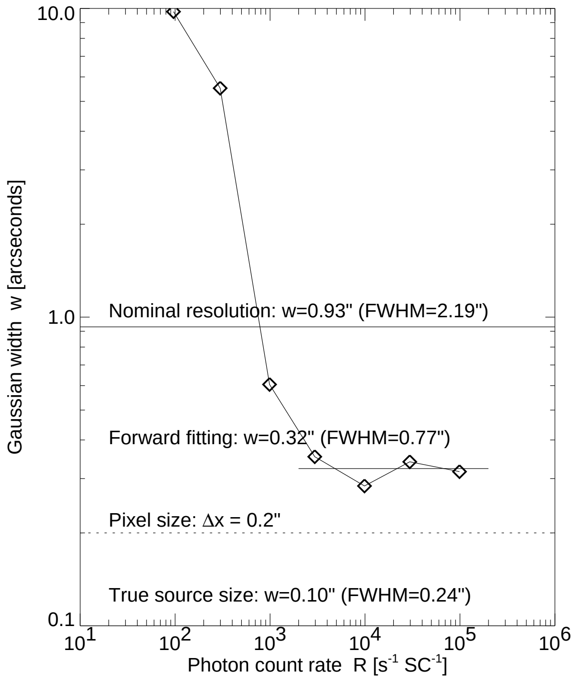


Fig. 10.— The forward-fitting results of 7 simulations with an unresolved source (with a gaussian width of $w_1 = 0.1$") are shown, reaching an asymptotic limit of $w_1^{fit} = 0.32" \pm 0.03"$. Note that this value is a factor of 3 below the nominal resolution.

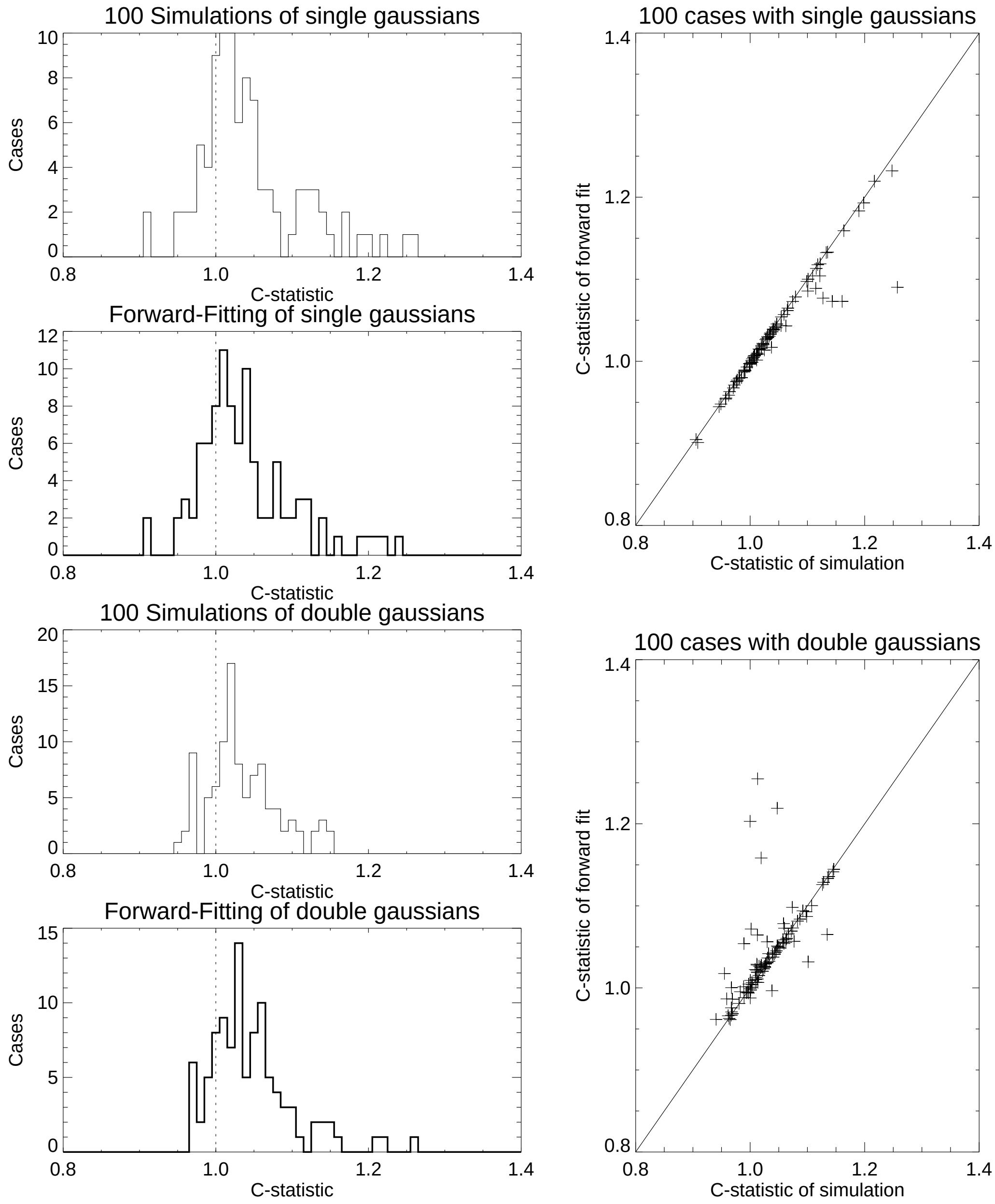


Fig. 11.— The values of the C-statistic are shown for the 100 simulations with a single gaussian and for the 100 simulations with double gaussians, both ranging around $0.95 \lesssim C \lesssim 1.1$. The values of the C-statistic obtained in the final convergence phase of the forward-fitting algorithm are shown in comparison, in form of histograms (left panels) and in form of scatterplots (right panels). Note the consistent match of the C values for most of the cases, indicating that the C-value is determined by the intrinsic data noise rather than by the convergence behaviour of the forward-fitting algorithm.

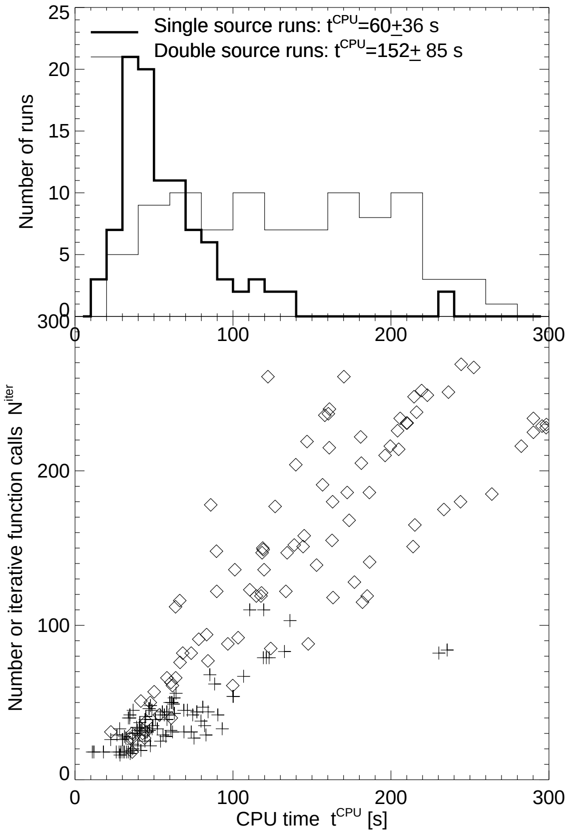


Fig. 12.— The computation times for 200 simulations with single sources (crosses and thick histogram) and double sources (diamonds and thin histogram) are shown, averaging to $t^{CPU} = 60 \pm 36$ s for single sources, and to $t^{CPU} = 152 \pm 85$ s for double sources, measured on a *SGI* workstation. Note that the CPU time is roughly proportional to the number of iteration function calls $n^{iter}$ of modulation profiles.